A STUDY ON THE EFFECT OF WATER DAMAGE TO FRACTURE CONDUCTIVITY IN THE MERAMEC SHALE

A Thesis

by

RYAN ARTHUR WINNER

Submitted to the Office of Graduate and Professional Studies of
Texas A&M University
in partial fulfillment of the requirements for the degree of

MASTER OF SCIENCE

Chair of Committee,	Ding Zhu
Committee Members,	A. Daniel Hill
	Benchun Duan
Head of Department,	Jeff Spath

August 2018

Major Subject: Petroleum Engineering

ABSTRACT

The goal of this study is to measure fracture conductivity on samples from the Meramec formation, a new unconventional play in Oklahoma. Conductivity samples were sourced from unpreserved downhole core provided by Marathon Oil. The scope of this investigation focused on the effect of produced water on the formation rock and the reduction in fracture conductivity after water exposure. Complementing these tests, each fracture was scanned using a surface profilometer to measure topagraphy, surface area, and roughness, and bulk mineralogy analysis utilizing x-ray diffraction (XRD) was conducted to correlate degree of water impairment to clay composition. In addition, a sieve analysis of the sand was conducted pre- and post-test to determine the amount of proppant crushing.

Tests were conducted using a Modified API RP-61 conductivity apparatus that permits dry nitrogen and reconstituted brine to be flowed through the system. Water conductivity tests were conducted using two different proppant concentrations, 0.2 lb/ft^2 and 0.4 lb/ft^2, and three sizes of proppant used by Marathon in the field, 20/40, 30/50, and 40/70 mesh sand. A reconstituted brine, representing flow back water, was made from salinity results from a third-party vendor used by Marathon.

Unrecoverable loss of conductivity due to water damage ranged from 24 to 54 percent for the 0.2 lb/ft^2 samples, and 16 to 62 percent for 0.4 lb/ft^2 samples. It was found that fracture surface topography played an important role in fracture conductivity, and that significant proppant crushing occurred. Additionally, mineralogy was found to vary significantly along the core depth interval, but results were inconsistent when compared to previous studies performed on the Eagle Ford and Barnett formations. These tests provide preliminary results for the Meramec formation, and how water damage affects fracture conductivity.

DEDICATION

To Rick and Lorene, who have provided unwaivering support and encouraged me to find my path no matter what the challenge. For Pop-Pop, Nannie, Goong-Goong, and Po-Po, who were essential to making my education possible. And to Christopher, who doesn't know all the fun he's missing in Grad school.

ACKNOWLEDGMENTS

First of all I would like to thank Dr. Zhu and Dr. Hill for providing me the opportunity to work under their research group. Over the past year and a half they have provided me the opportunity to work on two research projects focused on formations at the forefront of the oil industry. These projects and our weekly and monthly group meetings have helped further my knowledge of hydraulic fracturing, and for their insight and confidence shown in me I am forever grateful. I would also like to thank Dr. Benchun Duan for serving as a committee member, and for sharing his wealth of knowledge in geomechanics.

Special thanks to Mr. John Maldonado for all the help provided in the lab and in finding tools, even when it was most inconvenient. I would also like to thank Kevin Wiley and James Fernandez for our discussions in the lab that helped me become intimately familiar with the conductivity setup. Extra special considerations go to Dr. Dante Guerra and Jesse Guerra, two of the best Ph.D. mentors a new Master's student could ask for. For the countless hours spent in the lab, and many inspiring Friday and Saturday night discussions. I would also like to thank the previous members of the fracture conductivity group for laying the groundwork for these experiments.

Lastly, I'd like to thank the guys at 3910 S. College who made the transition from Pittsburgh to Texas much more bearable.

CONTRIBUTORS AND FUNDING SOURCES

Contributors

This work was supported by a thesis committee consisting of Advisor, Dr. Ding Zhu, and Dr. A. Daniel Hill of the Harold Vance Department of Petroleum Engineering and Dr. Benchun Duan of the Department of Geology and Geophysics.

The data analyzed for the XRD Analysis in Chapter 3 was provided by Dr. Nasr-El-Din's group. The source code for the Surface Scan and Roughness outputs, along with technical assistance during the experiments were generously provided by PhD Candidate Jesse Guerra from Dr. Zhu's conductivity group.

All other work conducted for the thesis was completed by the student independently.

Funding Sources

Graduate study was supported by a fellowship from Texas A&M University and a Research Assistant position for the Meramec Conductivity experiments was funded by Marathon Oil Company.

NOMENCLATURE

beta	Inertial term for Forcheimer equation
C_f	Fracture conductivity (mD-ft)
$C_{f,recovered}$	Recovered fracture conductivity post-water (mD-ft)
ΔP	Differential pressure through fracture (psi)
h_f	sample width (in)
hhp	Hydraulic horsepower
ISO	International Organinzation for Standardization
k_f	fracture permeability (mD)
L	Length of flow path (in)
$\dot{M}$	Mass flow rate (kg/s)
M_g	Molecular weight of gas (kg/mol)
μ	Viscosity (cP, Pa s)
P_{cell}	Average pressure within fracture (psi)
ppm	Parts per million
R	Universal gas constant (J/mol K)
ρ_f	Fluid density (kg/m^3)
SA_{frac}	Fracure surface area (in^2, ft^2)
STACK	Sooner Trend Anadarko Basis Canadian and Kingfisher Counties
T	Temperature (K)
v	Fluid velocity (m/s)
w_f	Fracture width (in)

XRD	X-Ray Diffraction
Z	Gas compressibility factor

TABLE OF CONTENTS

Page

ABSTRACT ii

DEDICATION iii

ACKNOWLEDGMENTS iv

CONTRIBUTORS AND FUNDING SOURCES v

NOMENCLATURE vi

TABLE OF CONTENTS viii

LIST OF FIGURES xi

LIST OF TABLES xiv

1. INTRODUCTION AND LITERATURE REVIEW 1

1.1 Background 1
1.2 Geology of the Meramec Formation 1
1.3 Literature Review 3
1.3.1 Hydraulic Fracturing 3
1.3.2 Fracture Conductivity 5
1.3.2.1 Modified API Fracture Conductivity Cell 6
1.3.3 Parameters Affecting Fracture Conductivity 7
1.3.3.1 Surface Roughness 7
1.3.3.2 Mineralogy 8
1.3.4 Water Damage and Fracture Conductivity 9
1.4 Objective of Study 10
1.5 Thesis Outline 10

2. EXPERIMENTAL DESIGN AND METHODOLOGY 12

2.1 Fracture Conductivity Sample Preparation 12
2.1.1 Sample Fracturing 13
2.1.2 Surface Profile Scan 14
2.1.3 Proppant Loading and Sample Coating 15
2.2 Flowback Water Reconstitution 17

2.3 Laboratory Procedures 18
2.3.1 Apparatus 19
2.3.1.1 Modified API Conductivity Cell 19
2.3.1.2 Load Frame 20
2.3.1.3 Water Pump 22
2.3.1.4 Nitrogen Flowmeter 23
2.3.1.5 Differential and Cell Pressure Sensors 23
2.3.1.6 Nitrogen Tank and Pressure Valve 24
2.3.2 Experimental Design 25
2.3.2.1 Gas Conductivity Calculation 25
2.3.2.2 Water Conductivity Calculation 29
2.3.3 Methodology of Water Fracture Conductivity Test 30
2.3.3.1 Nitrogen Pre-Water 30
2.3.3.2 Water Stage 33
2.3.3.3 Nitrogen Flow Post-Water 35
2.3.3.4 Disassembly 36

3. RESULTS 37

3.1 Sample Surface Scan and Roughness Results 37
3.1.1 Surface Scan of 0.2 lb/ft^2 Tests 37
3.1.2 Surface Scan of 0.4 lb/ft^2 Tests 40
3.2 Fracture Conductivity Water Test 42
3.2.1 Conductivity for 0.2 lb/ft^2 Tests 43
3.2.2 Conductivity for 0.4 lb/ft^2 Tests 46
3.3 XRD Mineralogy Results 49
3.4 Sieve Analysis Results 55

4. DISCUSSION OF RESULTS 59

4.1 Significance of Surface Roughness and ΔZ Results 59
4.2 Channeling of Proppant 61
4.3 Proppant Crushing 63
4.4 Impact of Repeated Sample Use 65
4.5 Mineralogy and Brittleness in Shales 70
4.6 Predicting Conductivity Due to Water Impairment 75

5. CONCLUSIONS 80

5.1 Recommendations 81

REFERENCES 83

APPENDIX A. APPENDIX A 87

A.1 Brittleness Results..... 87

LIST OF FIGURES

FIGURE Page

1.1 Geological timescale of Meramecian series deposition. Reprinted from Rottmann (2011). 2

1.2 Proppant scheduling throughout fracture treatment. Reprinted from Montgomery and Smith (2015). 4

2.1 Samples circled in red were chosen as fracture conductivity samples for this study. 12

2.2 Example of fractured sample provided by Kochurek Industries. 14

2.3 Laser profilometer used for surface scans of conductivity samples. 14

2.4 LabView software used to program each surface scan. 15

2.5 Workflow of experiments. 19

2.6 Components of the Modified API conductivity cell. 20

2.7 GCTS load frame used to apply closure stress for experiments. 21

2.8 CATS Standard window used to display test data in real time. 21

2.9 ISCO 500HP syringe pump used to pump reconstituted brine solution into the fracture. 22

2.10 Aalborg flowmeter used to measure volumetric flow rate of nitrogen. 23

2.11 Both transducers for P_{cell} and ΔP are Validyne DP 15 transducers. 24

2.12 Nitrogen source tank is attached to a regulator valve reducing pressure to working pressure in the fracture. 25

2.13 Measurements for port openings, and correct wrapping of Teflon tape to aid in sealing sample in conductivity cell. 31

2.14 Completed conductivity cell assembly with sample placed inside. 32

2.15 Fully assembled line connections for water fracture conductivity test. 34

3.1 Laser profilometer surface scan of 0.2 lb/ft^2 20/40 mesh sample. 37
3.2 Laser profilometer surface scan of 0.2 lb/ft^2 30/50 mesh sample. 38
3.3 Laser profilometer surface scan of 0.2 lb/ft^2 40/70 mesh sample. 39
3.4 Laser profilometer surface scan of 0.4 lb/ft^2 20/40 mesh sample. 40
3.5 Laser profilometer surface scan of 0.4 lb/ft^2 30/50 mesh sample. 41
3.6 Laser profilometer surface scan of 0.4 lb/ft^2 40/70 mesh sample. 42
3.7 Water Conductivity plot for 0.2 lb/ft^2, 20/40 mesh. 44
3.8 Water Conductivity plot for 0.2 lb/ft^2, 30/50 mesh. 45
3.9 Water Conductivity plot for 0.2 lb/ft^2 40/70 mesh. 46
3.10 Water Conductivity plot for 0.4 lb/ft^2, 20/40 mesh. 47
3.11 Water Conductivity plot for 0.4 lb/ft^2, 30/50 mesh. 48
3.12 Water Conductivity plot for 0.4 lb/ft^2, 40/70 mesh. 49
3.13 Mineralogy results for Sample 1..... 50
3.14 Mineralogy results for Sample 2..... 51
3.15 Mineralogy results for Sample 3..... 52
3.16 Mineralogy results for Sample 4..... 53
3.17 Mineralogy results for Sample 5..... 54
3.18 Mineralogy results for Sample 6..... 55
3.19 Pre- and post-test sieve analysis results for 20/40 mesh sand. 56
3.20 Pre- and post-test sieve analysis results for 30/50 mesh sand. 57
3.21 Pre- and post-test sieve analysis results for 40/70 mesh sand. 58
4.1 Fracture surface roughness versus initial fracture conductivity measurement... 60
4.2 ΔZ of fracture surface versus initial fracture conductivity measurement. 61

4.3 4.3a illustrates the even dispersion of proppant over the fracture face before testing. 4.3b shows the flow pathway formed by proppant channeling at 1000 psi closure stress. 62

4.4 Left image is initial proppant loading of sample, followed by channeling effect seen in picture on right. Reprinted from Guerra et al. (2017a). 63

4.5 Degree of proppant crushing versus decline in conductivity for first gas stage. 65

4.6 Fracture conductivity reuse plot for 0.2 lb/ft^2 20/40 mesh sand. 66

4.7 Fracture conductivity repeated test plot for 0.4 lb/ft^2 20/40 mesh sand. 66

4.8 Fracture conductivity reuse plot for 0.2 lb/ft^2 30/50 mesh sand. 67

4.9 Microscope image of fracture surface post-test. Note the embedded sand crystals on the right side of the image. 68

4.10 Fracture surface top and bottom, note the white coloration of the fracture surface due to sand crystals adhered to rock after sample cleaning. 69

4.11 Comparison between Meramec core samples and previous studies on the Barnett, Eagle Ford, and Marcellus Shales. 73

4.12 Trend for recoverable conductivity versus undamaged conductivity. Reprinted from Zhang et al. (2015) 76

4.13 Trend for recoverable conductivity versus undamaged conductivity for the Eagle Ford Formation. Adapted from Guerra (2018) 77

4.14 Trend for recoverable conductivity versus undamaged conductivity for the Marcellus Formation. Adapted from Guerra (2018) 77

4.15 Trend for recoverable conductivity versus undamaged conductivity for the Meramec formation. 78

LIST OF TABLES

TABLE Page

2.1 Renaming scheme for tested core samples. 13

2.2 Distribution of proppant loading for samples tested. 16

2.3 Mass of proppant needed for each respective load concentration. 17

2.4 Overview of salts needed to compose reconstituted brine solution. 18

4.1 Tabular values for roughness, R_{RMS} of the six core samples used in experiments. 59

4.2 Degree of proppant crushing for each mesh size. 64

4.3 Table of percent unrecoverable loss in conductivity for each core sample. 68

4.4 Summarized results for mineralogy analysis of Meramec, Barnett, Eagle Ford, and Marcellus Shales from lab data. 71

4.5 Wang and Gale BI results for Eagle Ford Shale. Reprinted from Enriquez-Tenorio (2016). 74

4.6 Wang and Gale Brittleness Index values for Meramec core samples. 74

A.1 Brittleness results for the Jarvie BI. 87

A.2 Brittleness results for the Kias BI. 88

1. INTRODUCTION AND LITERATURE REVIEW

1.1 Background

Although commonly labeled as a "new" technology in the oil and gas industry, hydraulic fracturing has successfully been used as a stimulation treatment since 1949 by Standolind Oil (Montgomery and Smith, 2010). Early hydraulic fracturing treatments used a gelled crude or kerosene mixture to propagate fractures in the reservoir, mainly due to concerns of formation damage due to water. Water, with chemical additives, was later used as a fracturing fluid in 1953. It was not until the 1990's that modern hydraulic fracturing became widely used in unconventional wells as a means to extend the contacted reservoir area, with the successful development of the Barnett shale by Mitchell Energy.

Hydraulic Fracturing is a stimulation technique for oil and gas wells where a perforated section of the wellbore is isolated and fluid is pumped downhole to initiate a fracture within the rock. Initially a pad, consisting of frac fluid without proppant, is pumped downhole to initiate a fracture and widen it sufficiently to allow proppant. Next, proppant, typically sand, is added to the fluid and pumped downhole to keep these fractures opened against the closure stress of the reservoir as it is propagated. In addition to sand, chemicals such as friction reducers are added to reduce friction as the fluid travels through the casing and pipe. For a well to produce, the fracture must be adequately propped to allow the transport of oil and gas to flow from the reservoir into the wellbore. Fracture conductivity is a measure of how restrictive a flow path is to a given fluid, thereby its study provides insight into how well a particular fracturing treatment will perform.

1.2 Geology of the Meramec Formation

The Meramec formation, deposited 340 to 355 million years ago, is a Mississipian age rock that is composed of Missouri Limestone and various carbonates along with interbedded

shales (Rottmann and Hadaway, 2012). The depositional environment of formation was in shallow, warm, and relatively quiet marine shelf waters (McKenna, 1979). The Meramec is bordered by the Osagean series below, and the Chesterian series above shown in Figure 1.1 (Rottmann, 2011). The Meramec is similar in appearance to the Osage, with the primary difference being an abundance of chert giving it a gray to dark gray appearance (McDuffie, 1958).

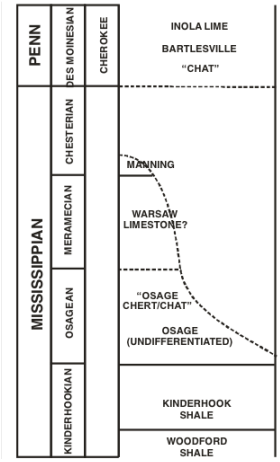

Figure 1.1: Geological timescale of Meramecian series deposition. Reprinted from Rottmann (2011).

The source rock for the Meramec is the Woodford Shale, where a combination of stratigraphic traps and lateral discontinuities act as a seal (McKenna, 1979). This formation is part of what is know as the STACK (**S**ooner **T**rend **A**nadarko Basin **C**anadian and **K**ingfisher Counties). This formation consists of highly impermeable rock. The core samples of this study are categorized as part of the shale formation. Mineralogy analysis results for these core sections are presented in Chapter III, and discussion of their significance follows in Chapter IV

1.3 Literature Review

This section will review the studies of fracture conductivity and previous research works on the impact of water on fracture conductivity.

1.3.1 Hydraulic Fracturing

Hydraulic fracturing has proved to be one of the most resilient technologies in the oil and gas industry. Since 1949 when the first fracturing treatment was initiated, over 2.5 million fracturing treatments have been pumped (Montgomery and Smith, 2015). While hydraulic fracturing has been a staple of the oil and gas industry in the past 15 years, it has constantly been progressing. One example is the introduction of slickwater fracturing. Slickwater uses water as the transport fluid, with clay stabilizers and friction reducer added. Due to the low viscosity of this fluid, proppant transport becomes a primary issue. The industry has addressed this with increased flowrates; where initial fracturing jobs were pumped at 2-3 bbl/min, current hydraulic fracturing treatments can be pumped in excess of 100 bbl/min to allow adequate proppant transport. Despite the high flow rates used for treatment, slickwater fracs use very low proppant concentrations, usually no more than 3 lb/gal, but it is capable of placing hundreds of thousands of pounds of proppant per stage (Palisch et al., 2010). In order to provide the power to pump this amount of fluid downhole, service companies have upgraded pumps to provide much more than the old average of 75 hhp, in some cases with as much as 15,000 hhp available (Montgomery and Smith, 2010). As stated by Montgomery and Smith (2010), the allure of hydraulic fracturing is its relatively low cost, ease of mixing, and treatments are repeatable. Additionally, hydraulic fracturing greatly increases the contacted reservoir area, often believed to create a complex fracture network, with a high potential to increase production.

Another evolution in hydraulic fracturing has been the type of proppant used. Originally screened river sand, but since then companies have shifted to higher, ISO quality sand due

in part to the fact that it is abundant and relatively inexpensive. Most sand sizes used in the industry for conventional reservoirs today are a 20/40 US-standard-mesh sand, with approximately 85% of jobs using this sand type (Montgomery and Smith, 2010), however use of 100 mesh sand has also increased recently due to its abundance in sand quarries. Along with natural sand, innovative proppants have been evaluated including steel shot, glass, resin coated sands, and ceramic. In addition to different sand types used, the proppant concentration schedule used in fracture treatments has evolved as well. Hydraulic fractures begin by pumping a pad fluid, or clean fluid, above the fracture pressure of the formation, which is then followed by pumping different concentrations of proppant. Early on, the idea of a mono layer or partial monolayer were seen as the ideal fracture treatment so proppant concentration remained low. In more recent years, proppant concentration has shifted to pumping a lower concentration just after the pad stage, and gradually increasing concentration as the treatment progresses, illustrated in Figure 1.2. In some cases proppant concentration near the end of the treatment can be as high as 20 lb/gal (Montgomery and Smith, 2010).

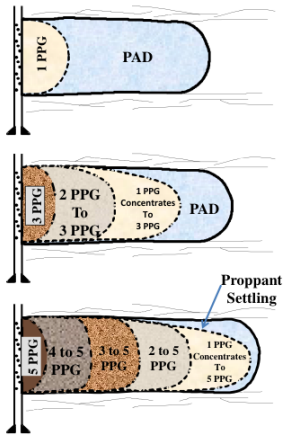

Figure 1.2: Proppant scheduling throughout fracture treatment. Reprinted from Montgomery and Smith (2015).

1.3.2 Fracture Conductivity

Modern testing of fracture conductivity for laboratory-based experiments rely on standard or non-standard ISO fracture conductivity tests. Standard tests are based on ideal, non-realistic conditions, where calculated fracture conductivity is dependent on proppant permeability and loading regimes. For these ideal tests there are two types of tests that dictate the time in which the experiment is run; API RP-61 and API RP-19. API RP-61 provides standards to conduct a short-term proppant pack experiment, while the API RP-19 standard dictates a long-term proppant pack conductivity . This experiment measures conductivity of a 2 lb/ft^2 proppant pack between two parallel Berea Sandstone cores in which 2% KCl brine is flowed through the fracture at a given closure stress. Although these experiments produce conductivities that are orders of magnitude larger than those seen in a real downhole fracture, they characterize the flow capabilities of the proppant (Economides et al., 2012).

Non-standard ISO fracture conductivity tests encompass any deviation from the standard practice, whether the fluid is changed, a different proppant concentration is used, or the fracture material is changed. While standard ISO tests primarily characterize flow through the proppant pack, the proposed modified ISO changes aim for a more realistic fracture condition by changing the proppant concentration, realistic test conditions, and using test samples other than Berea Sandstone. Ramurthy et al. (2011) details changes in test samples to include cylindrical core plugs, using a Hassler-type core holder, or rectangular shaped samples with rounded edges. These samples can be saw cut or have an induced rough surface via fracturing or other means.

Some proposed changes include Cooke Jr (1973) who investigated the effect of non-Darcy flow of brine at an elevated temperature and concluded that conductivity values are lower than that of a standard API test. Cooke in 1975 also determined that fracturing fluid properties such as residue and their interaction with proppant has a significant effect on

fracture conductivity. It should be noted that Cooke's work studying these effects utilized a conductivity cell that served as the basis for modern Standard API Conductivity Cells (Zhang, 2014). Among other variations of the Standard API practices, studies focusing on dynamic proppant placement to mimic injection of proppant into a fracture have been conducted (Marpaung et al., 2008). In addition to these independent modifications to the Standard API practice, commercial company Stim-Lab, currently known as Core Laboratories, has conducted numerous conductivity tests to create a software that modifies the Standard API fracture conductivity test results to account for damage mechanisms (Zhang, 2014).

1.3.2.1 Modified API Fracture Conductivity Cell

The Modified API Conductivity Cell adapts the Standard API Fracture Conductivity Cell first used by Cooke to allow testing of a more realistic fracture environment. The procedure for experiments on this modified conductivity cell are governed by the procedures outlines in API RP-61 for a short-term conductivity test. The main deviation from the Standard API conductivity cell lie in the sample dimensions, utilizing a taller specimen to allow for leak off applications. Sample dimensions for the modified conductivity cell are 7.10 inches long with rounded edges, 1.61 inches wide, and 6 inches high. Dependent upon the source dimensions from which the sample is obtained, the shale portion at a minimum is 2.5 inches thick but can span the entire 6 inch thickness required for a complete sample. Should the shale portion fall short of the 6 inch requirement, sandstone inserts are used to complete the dimensions of the fracture conductivity sample.

By using a shale or mudrock sample, the Modified API conductivity cell provides an advantage of using real formation rock. A fracture is induced on the shale portion, providing a rough surface akin to what is expected of a propagated fracture downhole instead of smooth, parallel plates. Rather than testing proppant pack conductivity, proppant concentrations used in the field for a particular formation are used, effectively testing the permeability through

the fracture. Instead of flowing 2% KCl, dry nitrogen is flowed through the fracture which does not damage the formation rock, although the cell allows for brine to be flowed through the cell if desired. In addition, the length of the sample provides sufficient space for flow development while the sample surface area is kept the same as the API/ISO standard. This effectively allows for direct comparison with results from Standard API conductivity tests.

1.3.3 Parameters Affecting Fracture Conductivity

This section covers the previous work done on the parameters of interest for this study. These parameters include surface roughness, mineralogy, proppant crushing and embedment, and self channeling of proppant.

1.3.3.1 Surface Roughness

Studies have shown that fracture surface roughness can have a significant effect on the resulting conductivity through a fracture. Thompson and Brown (1991) investigated anisotropic effects of fracture surface roughness using a synthetically created rough fracture by flowing water. It was found that roughness orientation transverse to fluid flow resulted in a fluid velocity lower than the mean velocity, while roughness oriented parallel to flow aided the transport of fluid. Knorr (2016), found that for unpropped fracture conductivity samples fracture conductivity is dictated by surface roughness. The larger the roughness, the higher the conductivity of the fracture. The fracture surface displacement from this roughness was found to provide a sufficient pathway for fluid conductivity through the fracture (Fredd et al., 2001). Likewise, it has been found that fracture surface roughness influences propped conductivity (Kassis and Sondergeld 2010; Enriquez-Tenorio 2016). Surface roughness for propped conductivity experiments, measured as the root-mean-square asperity heights, influence initial fracture conductivity and have less of an impact at later load stages. Additionally, Enriquez-Tenorio (2016) found that while high surface roughness primarily effects the initial conductivity, high surface area correlates with higher conductivity values at larger closure

stresses. Zhang (2014) found that roughness on a sloped surface of the fracture contributes to the degradation of a monolayer of sand proppant at higher closure stresses.

1.3.3.2 Mineralogy

Mineralogy and its impact on fracture conductivity have been studied extensively for unconventional reservoirs. The most common conductivity sample attribute using mineralogy is to calculate brittleness on a mineralogical basis. Rickman et al. (2008) found that for shale samples, the amount of quartz in a sample has a direct correlation to brittleness. Another qualitative description of shale brittleness has been proposed by Sone and Zoback (2013). This characterization is composed of "soft" layers containing kerogen and clay, and "stiff" layers containing carbonates, quartz, and feldspars. The idea of "soft" and "stiff" layers proposed by Sone and Zoback has been supported by various studies (Li et al. 2015; Fjær and Nes 2013). Along with the previously mentioned qualitative descriptions of shale brittleness, there are a great number of mineralogical-based brittleness indices(BI). One of the more prominent brittleness indices was proposed by Jarvie et al. (2007) while studying the Barnett shale formation. Due the the high quartz content found throughout this mudstone, the brittleness for this index is largely dependent on quartz content. Equation 1.1 shows the Jarvie BI, where Q is quartz content, C is carbonate content, and Cl is clay content of the rock.

$$BI = \frac{Q}{Q + C + Cl} \tag{1.1}$$

Wang and Gale (2009) modified the Jarvie BI to include dolomite which they found to increase brittleness, and total organic content (TOC) which Wells (2004) found to increase ductility of the rock. Equation 1.2 shows the Wang and Gale BI where Dol is dolomite content, TOC is total organic content, and Lm is limestone, which is less brittle than dolomite.

$$BI = \frac{Q + Dol}{Q + Dol + Lm + Cl + TOC} \tag{1.2}$$

Another well known brittleness index is the Kias BI (Kias et al., 2015). For this index, Kias et al. determined that quartz, k-feldspar, dolomite, calcite, and plagioclase were the primary minerals that increase brittleness in mudstones. The Kias BI is shown in Equation 1.3 where *V* indicates weight fraction of a mineral, *QTZ* is quartz, *SID* is siderite, *CAL* is calcite, *PLA* is plagioclase, and *KSP* is k-feldspar.

$$BI = \frac{V_{QTZ} + V_{PLA} + V_{CAL} + V_{KSP} + V_{DOL}}{V_{QTZ} + V_{PLA} + V_{CAL} + V_{KSP} + V_{DOL} + V_{SID} + V_{CLAY}} \tag{1.3}$$

While each of these indices are widely accepted by the scientific community, it remains an issue to relate these indices to each other due to the definition of brittleness for each.

1.3.4 Water Damage and Fracture Conductivity

The influence of fluid impairment on fracture conductivity dates back to 1975 when Cooke studied the effect of fracturing fluids. Since then, work has been conducted utilizing realistic downhole conditions investigating the effects of slickwater fracturing (Palisch et al., 2007), the effect of fracturing fluids on rock mechanical properties (Akrad et al., 2011), and the sensitivity of fluid interactions in shales (Ramurthy et al., 2011).

More recent work has focused on water-rock interactions in specific shale formations. It has been found that the interactions between water and rock can be physical, chemical, or a combination of both (Civan, 2015). Zhang (2014) quantified the conductivity loss due to water damage in the Barnett formation. It showed that conductivity loss was significantly impacted, up to 80 percent, by excessive proppant embedment due to softening of the fracture surface after exposure to water. Further studies on the Eagle Ford and Marcellus formations have shown a direct relationship between high clay content and unrecoverable loss in conductivity. Conductivity reduction due to water damage ranged from 4 to 25 percent for the

Eagle Ford shale, and 36 to 48 percent loss in conductivity in the Marcellus shale. Guerra et al. (2017b) presented a study that showed an inverse relationship between fracture surface topography and unrecoverable loss in conductivity. This relationship applies to all of the studied shale formations, namely the Eagle Ford, Barnett, Marcellus, and Bakken Shales.

1.4 Objective of Study

The focus of this study is to characterize the effects of water on fracture conductivity of downhole Meramec core. This is the first study of its kind on this formation, and results of all tests and analyses will help to characterize this formation. Primary areas of focus are the effects of water impairment, mineralogy of the formation throughout the depth interval provided, fracture surface area and roughness, and any mechanical properties. The focus of this study is to quantify the unrecoverable loss in conductivity in the Meramec formation, and seek the formation attributes that drive the loss in conductivity due to water damage by analyzing mineralogy and mechanical properties of the core samples. Once these values have been quantified, a comparison will be made to evaluate the Meramec formation and its place among the top unconventional plays that have been evaluated by this research group.

1.5 Thesis Outline

The background to hydraulic fracturing, experimental history of fracture conductivity, study of water interactions on fracture conductivity, and the objective and approach of this study were covered in Chapter 1.

Chapter 2 discusses experimental apparatus and procedures, including sample preparation, flowback brine reconstitution, and laboratory procedures. More specifically, sample preparation will cover topics such as sample fracturing, proppant loading and epoxy coating, and laser surface scanning. Laboratory procedures will detail the various equipment used for fracture conductivity experiments, how fracture conductivity is calculated, along with a step-by-step procedure of the water conductivity test.

Chapter 3 will present the results for the various analyses conducted in conjunction with the water conductivity experiment. Such analyses include surface area and surface roughness, x-ray diffraction (XRD) mineralogy analysis, proppant sieve analysis, and mineralogy-based brittleness results.

Discussion of these results and findings will be covered in Chapter 4.

Chapter 5 will discuss the conclusions of the study as well as recommendations for future work on the Meramec formation.

2. EXPERIMENTAL DESIGN AND METHODOLOGY

This chapter will cover the Methodology of a water fracture conductivity experiment. Sample preparation will be covered along with laboratory procedures for conductivity testing.

2.1 Fracture Conductivity Sample Preparation

The samples for this study were sourced from unpreserved downhole core from the Rosemary 4-H well. Figure 2.1 shows the vertical location, based on measured depth (MD), for 21 individual core samples along a depth interval ranging from 9600 to 9735 feet deep. Candidate samples for fracture conductivity experiments, shown as the red circles in Figure 2.1, were chosen to cover the entire interval.

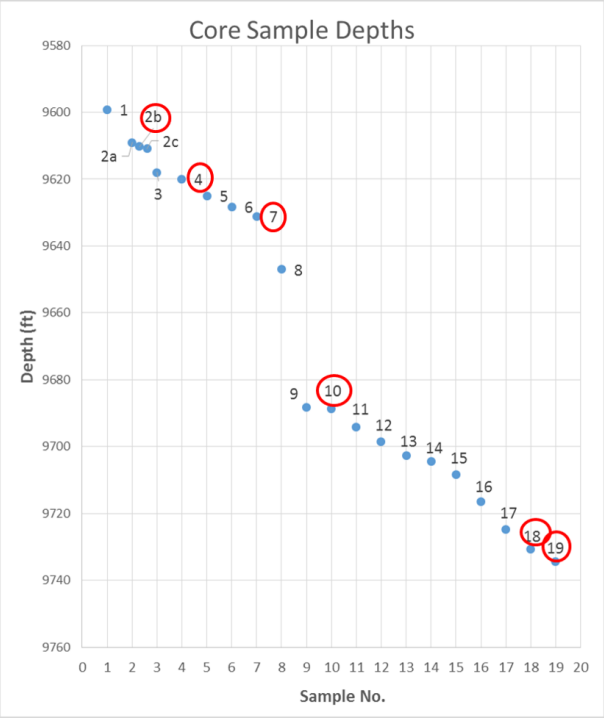

Figure 2.1: Samples circled in red were chosen as fracture conductivity samples for this study.

For the sake of simplicity, the samples were renamed from their respective depth interval number to 1 through 6, as shown in Table 2.1.

Depth Interval No.	Sample No.
2b	1
19	2
18	3
7	4
4	5
10	6

Table 2.1: Renaming scheme for tested core samples.

2.1.1 Sample Fracturing

Once samples were chosen, the cores were sent to Kochurek Industries where the cores were cut to the dimensions of the Modified API conductivity cell (1.65 inches wide, 7 inches long, and about 3 inches thick), and a fracture was induced on each core sample. Once the core has been cut to shape, two steel sleeves are centered on the sample and a fracture is induced under mode I tension. Figure 2.2 shows a fractured core using this method. Care is taken to ensure any debris resulting from the fracture is not lost. After the sample is fractured, two Berea sandstone inserts are paired with the fractured halves to ensure the fracture surface will be centered in the conductivity load cell, and the required height of 6 inches for the conductivity cell.

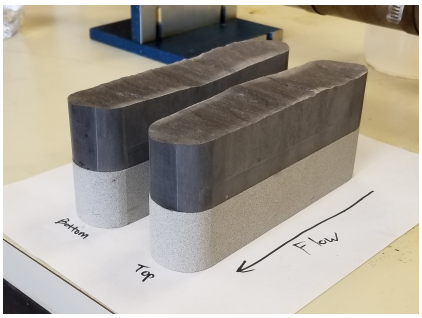

Figure 2.2: Example of fractured sample provided by Kochurek Industries.

2.1.2 Surface Profile Scan

After the fractured samples are created, the two halves are analyzed to determine top and bottom and which side is best suited to face the pressure ports of the apparatus. Direction of flow for each sample is determined by the fracture orientation; the inlet side was chosen such that the fracture was centered along the thickness. After the inlet side has been designated, each half is scanned using a Laser Profilometer pictured in Figure 2.3, using the denoted flow orientation as a reference for meshing the resulting surface images.

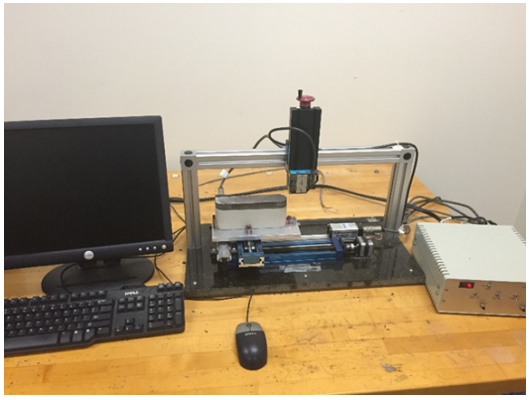

Figure 2.3: Laser profilometer used for surface scans of conductivity samples.

The plate on which the sample is placed can move in both the x- and y-directions, while

the laser measures the z-direction or height of the sample at a single point. Prior to initializing the data acquisition software, the laser module was adjusted such that the lowest and highest points on the sample did not exceed its measurement range. Using a LabView control program, the length and width of the sample are specified along with the measurement interval as shown in Figure 2.4. For each of the six samples tested, a measurement interval of 0.025 inch was used. Data was later interpreted using an in-house MATLAB code to plot surface topography, and calculate roughness and surface area.

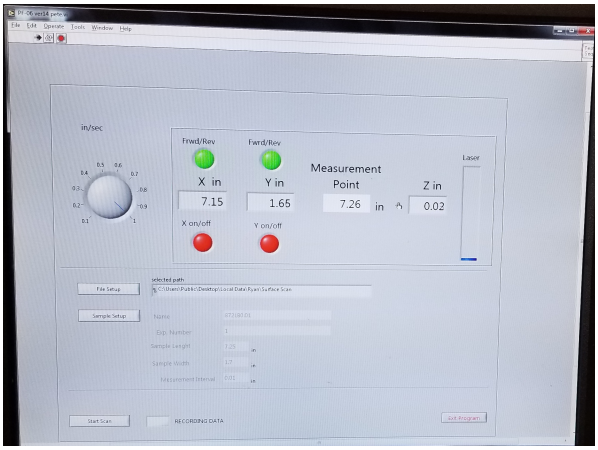

Figure 2.4: LabView software used to program each surface scan.

2.1.3 Proppant Loading and Sample Coating

Proppant concentrations for tests were selected on the concentrations used in the field practice in Meramec hydraulic fracture treatments. Two proppant loads were used among three different mesh types of HiCrush sand. Table 2.2 shows the proppant specifications for each of the six core used in this study.

Sample No.	Sand Concentration (lb/ft^2)	Sand Size (Mesh)
1	0.2	20/40
2	0.2	30/50
3	0.2	40/70
4	0.4	20/40
5	0.4	30/50
6	0.4	40/70

Table 2.2: Distribution of proppant loading for samples tested.

Given a known proppant concentration, the surface area of the fracture must be calculated to determine the mass of proppant needed for each load, 0.2 lb/ft^2 and 0.4 lb/ft^2. Assuming a planar fracture area, the total surface area covered by proppant, in ft^2, is shown below.

$$SA_{frac} = A_{circle} + A_{rectangle} \tag{2.1}$$

Plugging in the values for conductivity sample measurements into Equation 2.1 yields:

$$SA_{frac} = \frac{\pi}{4} * \left(\frac{1.65}{12}\right)^2 + \frac{1.65in * (7 - 1.65in)}{144} = 0.0762ft^2 \tag{2.2}$$

With a total fracture area of 0.0762 ft^2, as shown in Equation 2.2, the mass of proppant for each load concentration can be calculated. These values are shown below in table 2.3.

Proppant Concentration (lb/ft^2)	Mass Proppant (g)
0.2	6.81
0.4	13.62

Table 2.3: Mass of proppant needed for each respective load concentration.

For each sample, the appropriate weight of sand is measured and distributed evenly along the surface. It should be noted that the fractured surfaces are not completely smooth, and there are topography changes along the surface. Due to the spherical shape of the sand grains, the sand would tend to aggregate in the lower parts of the bottom surface. Once proppant is evenly distributed, the top half of the fracture is carefully placed and blue painter's tape is applied to seal the sample to ensure the epoxy coating does not leak into the fracture void.

The epoxy resin coating is a two stage process. The first stage is to coat the sample with a primer to enhance the adhesion to the sample. The sample was coated three times, with 15 minute intervals between each coating. Next, the sample mold is coated with a silicon-based spray to aid in removing the sample. Once the primer has dried, the sample is placed in the mold, and was bolted together. The sample was centered and the mixed epoxy was slowly poured down one side. This was to ensure air bubbles would not become trapped, causing pathways for leakage. Upon completely filling the mold, the assembly was carefully placed inside an oven and allowed to cure at 125^oF for 4 hours. The sample was then removed from the mold and prepared for the conductivity test, which will be discussed later in this section.

2.2 Flowback Water Reconstitution

The reconstituted brine solution used for the water stage of the experiment was provided by Marathon Oil through Pay Rock Energy. Water chemistry results were conducted

by Jacam Laboratories. The total dissolved solids of this brine solution was 89,751 ppm, with sodium, calcium, and chloride as the primary ions present. Secondary ions present include magnesium, sulfate, potassium, bicarbonate, and strontium with trace amounts of iron. Figure 2.4 shows a tabulated version of the brine results and the conversion from parts per million of each ion, values in the second row, to lab units of grams per liter of its salt form, shown in the right-hand column.

	Ca^{2+}	Mg^{2+}	Sr^{2+}	Na^{+}	K^{+}	Al^{3+}	Fe^{2+}	Cl^{-}	SO_4^{2-}	HCO_3^{-}	Salt Needed (g/L)
Req. Conc.	3230.2	702	441.7	29314.3	329.9	1.17	95.3	56099.2	449.2	134	
$CaCl_2$	3230							5714			6.09
NaCl				29264				45124			74.39
KCl					330			299			0.63
$Fe(II)SO_4$							95		164		0.26
$MgSO_4$		72							286		0.36
$AlCl_3$						1		5			0.01
$MgCl_2$		630						1837			2.47
$NaHCO_3$				50						134	0.18
$SrCl_2$			442					357		0	0.80

Table 2.4: Overview of salts needed to compose reconstituted brine solution.

2.3 Laboratory Procedures

This section will cover the laboratory procedures that comprise the water conductivity experiment. Figure 2.5 shows the workflow from obtaining the core samples to data processing. This section will cover the equipment used for testing, the experimental design, and finally the step-by-step procedure on how to run a water conductivity test.

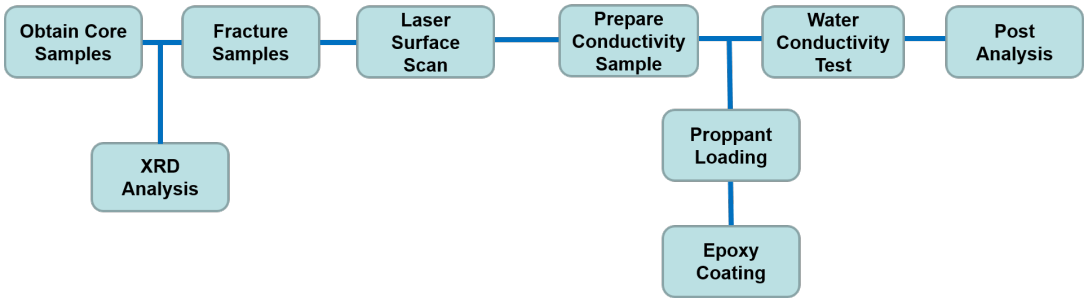

Figure 2.5: Workflow of experiments.

2.3.1 Apparatus

The water conductivity setup utilizes a variety of different equipment to measure values to calculate fracture conductivity. The key pieces of equipment are as follows:

- Modified API Conductivity Cell
- Load Frame
- Water Pump
- Nitrogen Flowmeter
- Differential and Cell Pressure Sensors
- Nitrogen Tank and Pressure Valve

2.3.1.1 Modified API Conductivity Cell

The modified API cell is constructed of stainless steel measuring 10 inches long, 8 inches thick, and 3.25 inches wide. The entire assembly consists of the cell, two flow inserts, and two pistons, as shown in Figure 2.6. The cell contains a cavity where a core sample 7 inches long, 1.65 inches wide and a maximum thickness of 7 inches can be loaded. Along the middle of the side of the cell are three pressure ports for cell pressure and differential

pressure transducers. The two flow inserts are made of stainless steel with threaded ports to allow a Swagelok fitting to connect flow lines. These two inserts connect upstream and downstream lines to the conductivity cell and have a viton polypak O-ring to seal the unit to the cell body. The two pistons are 7 inches long, 1.65 inches wide, and 3 inches thick, and are also made of stainless steel. Each piston has a threaded opening at the base that is connected internally to the piston surface in contact with the fracture to allow for fluid leak off capabilities. Both pistons also have viton polypak O-rings to aid in sealing the sample inside the conductivity cell.

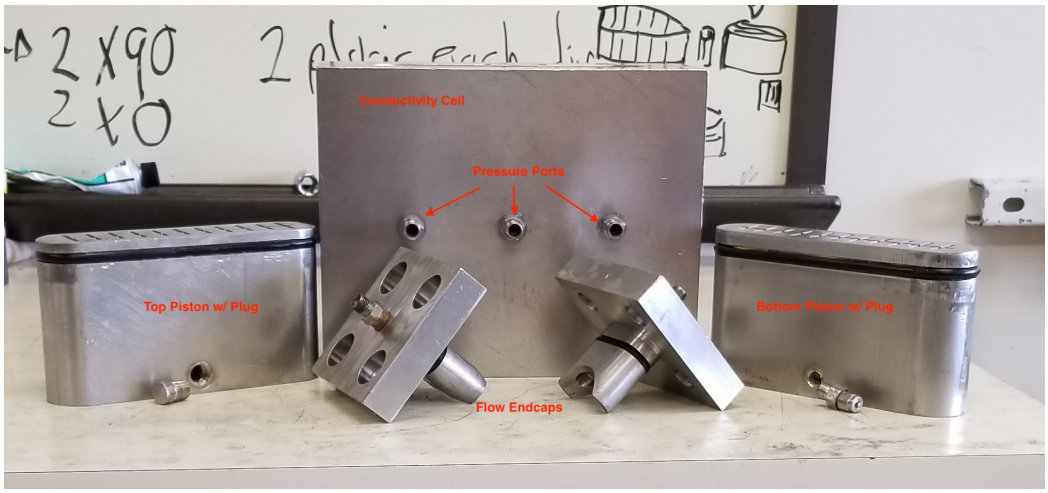

Figure 2.6: Components of the Modified API conductivity cell.

2.3.1.2 Load Frame

A GCTS UCT-1000 four column vertical load frame was used to conduct experiments. As shown in Figure 2.7, load is applied using a hydraulic pump connected to a mm piston. This frame is capable of a static load capacity of 1000 kN and a tension load capacity of 800 kN. The stroke of the piston is 100 mm, and maximum velocity is 80 mm per minute. Load is controlled by the GCTS CATS Standard software program displayed in Figure 2.8. The

four windows in the upper right side display the two pressure measurements, axial load, and axial displacement. In those four, the upper right window shows ΔP, the upper left displays P_{cell}, both in psi, the lower right displays axial load in kN, and the lower left displays axial displacement in mm. The bottom two plots display the values of these four measurements against time. The left plot displays axial load and displacement versus time, and the right plots ΔP and P_{cell} versus time.

Figure 2.7: GCTS load frame used to apply closure stress for experiments.

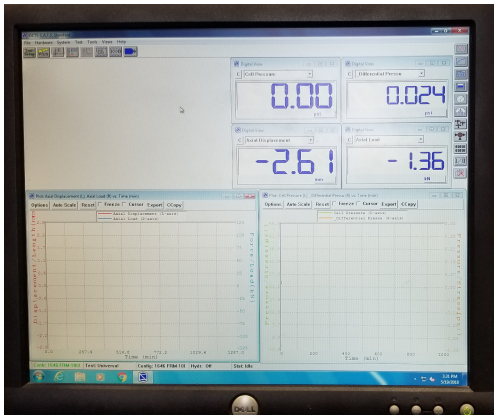

Figure 2.8: CATS Standard window used to display test data in real time.

2.3.1.3 Water Pump

Switching from Nitrogen, the reconstituted brine must be pumped into the system to register a pressure drop through the fracture. This is achieved through the use of a Teledyne ISCO 500HP syringe pump. Shown in Figure 2.9, this syringe pump has a total tank capacity of 500 mL, which is refilled from a 4 liter reservoir. Refilling and flow into the conductivity system is controlled by a Teledyne ISCO D Series Pump Controller. This controller allows for multiple settings from pumping at a pressure gradient, a constant pressure, or a constant flow rate. For this study, a constant flow rate of 2 mL per minute was used to establish a pressure drop through the fracture at 4000 psi closure stress.

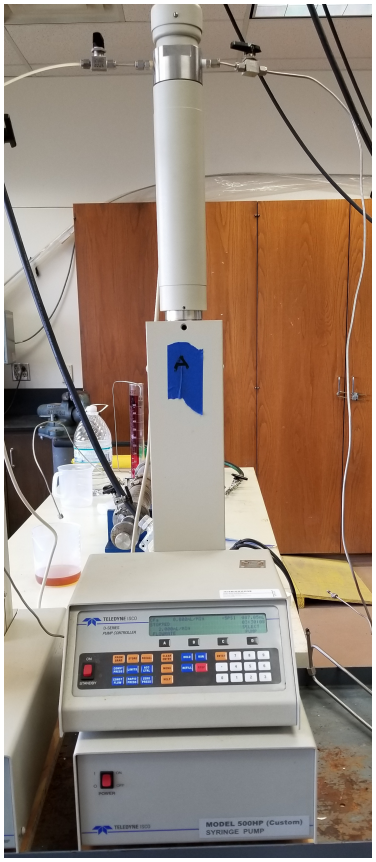

Figure 2.9: ISCO 500HP syringe pump used to pump reconstituted brine solution into the fracture.

2.3.1.4 Nitrogen Flowmeter

In order to measure the flow rate of nitrogen from the tank into the conductivity cell a flowmeter must be used. This system uses an Aalborg XFM Flowmeter, pictured below, which has a flow range rating from 0 to 10 liters per minute. The flowmeter is capable of measuring flow rate up to a working pressure of 500 psi. This particular flowmeter measures the temperature of the fluid passing through it, and uses correlations to calculate flow rate. As such, this flowmeter is calibrated for only nitrogen gas, and has a factory calibrated error of ±1% or ±100 mL per minute.

Figure 2.10: Aalborg flowmeter used to measure volumetric flow rate of nitrogen.

2.3.1.5 Differential and Cell Pressure Sensors

The sensors used to measure cell and differential pressure were Validyne DP 15 transducers, pictured in Figure 2.11. These sensors have interchangeable membranes rated to various pressure ranges. The cell pressure transducer utilized a *3-50* membrane rated to ±125 psi, while the differential pressure transducer used a *3-34* membrane rated to ±3.2 psi. The DP 15 transducers are factory calibrated to ±2.5% accuracy. Attached to these sensors are a Swagelok filter with a 90 μm filter membrane to prevent proppant from reaching the inside of the transducer, and the analog pressure gauges as quality assurance instruments.

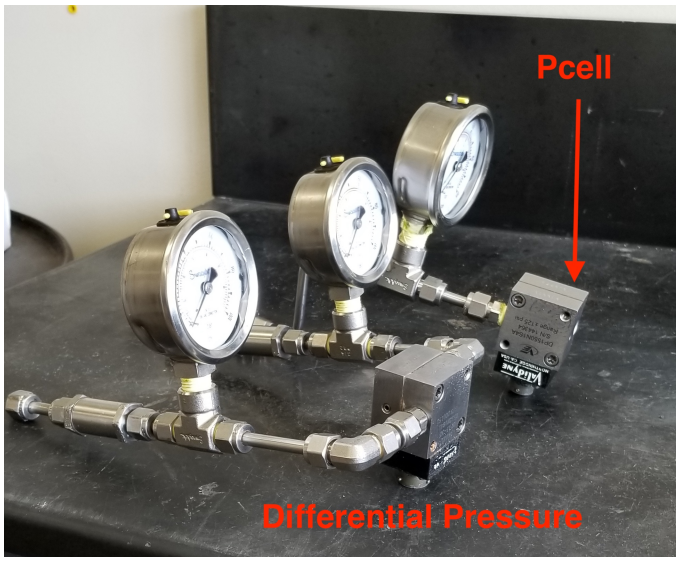

Figure 2.11: Both transducers for P_{cell} and ΔP are Validyne DP 15 transducers.

2.3.1.6 Nitrogen Tank and Pressure Valve

The first part of the water conductivity experiment is a non-destructive, meaning the rock is not damaged by the fluid, conductivity test. Nitrogen is supplied by a liter tank, where a control valve reduces the effective pressure to a value at which the test can be conducted. Figure 2.12 depicts the tank, with the brass control valve located at the top of the left tank. This control valve has gauges for high and low pressure and connecting the gauge to the conductivity system is a braided stainless steel flexible line.

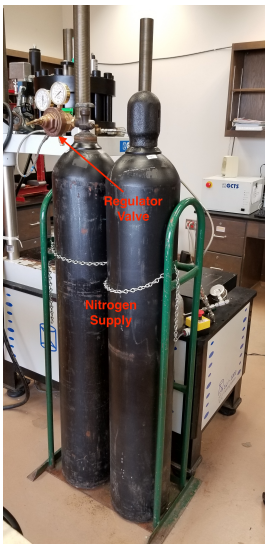

Figure 2.12: Nitrogen source tank is attached to a regulator valve reducing pressure to working pressure in the fracture.

2.3.2 Experimental Design

To calculate fracture conductivity for the water conductivity experiment there are two distinct calculations used. One is applied for flow of nitrogen gas through the fracture, and the other is for a reconstituted brine as the flowed fluid. The methodology to calculate each follows in the next two subsections.

2.3.2.1 Gas Conductivity Calculation

For the dry nitrogen stage of the experiment at a given closure stress, four flow rates and their respective cell pressure and differential pressures are recorded. Equations 2.3 and 2.4 show the Darcy equation and Forcheimer equation used to calculate conductivity using these recorded values.

$$-\frac{dp}{dL} = \frac{\mu v}{k_f} \tag{2.3}$$

$$-\frac{dp}{dL} = \frac{\mu v}{k_f} + \beta \rho_f v^2 \tag{2.4}$$

Where $-\frac{dp}{dL}$ is the pressure drop over a unit length, v is the fluid velocity, μ is the fluid viscosity, and k_f is the fracture permeability. The variables in the Forcheimer equation are β, the intertial factor, and ρ_f, the fluid density.

The Forcheimer equation is for turbulent flow rates with the second term acting as a correction factor for the Darcy equation. Zhang (2014) found that flow rates below 0.8 L/min at a proppant concentration of 0.1 lb/ft^2, the Darcy equation holds true, and flow rates above 0.8 L/min the Forcheimer equation should be used. More recently, McGinley (2015) found that flow rates below 2 L/min for concentrations up to 0.1 lb/ft^2, the Darcy equation is applicable. Likewise, for flow rates above 2 L/min the Forcheimer equation should be applied.

In order to use the Darcy equation for the laboratory experiments a combination of the ideal gas law, Darcy's law, and conservation of mass must be applied. To do this, Equation 2.3 is multiplied by fluid density, ρ_f.

$$-\frac{dp}{dL}\rho_f = \frac{\mu v}{k_f}\rho_f \tag{2.5}$$

Using the ideal gas law in terms of density,

$$\rho_f = \frac{pM_g}{ZRT} \tag{2.6}$$

Where p is pressure, M_g is molecular weight, R is the universal gas constant, T is temperature, and Z is the gas compressibility factor. In addition to the ideal gas law, a relationship between fluid density, mass flow rate, and fluid velocity is used.

$$\frac{\dot{M}}{A} = v\rho_f \tag{2.7}$$

Where $\dot{M}$ is mass flow rate and *A* is flow area. Rearranging Equation 2.7 for ρ_f and combining with Equation 2.5 and Equation 2.6 we get Equation 2.8

$$-\frac{pM_g}{ZRT}dp = \frac{\mu\dot{M}}{k_f A}dL \tag{2.8}$$

Integrating for *dP* and *dL* and rearranging we arrive at the following expression.

$$\frac{(P_1^2 - P_2^2)}{2}\frac{M_g}{ZRT} = \frac{\mu\dot{M}}{k_f A}L \tag{2.9}$$

Where *L* is the length of the flow path, P_1 is upstream pressure, and P_2 is downstream pressure. To use this equation in terms of the known variables P_{cell} and ΔP, we must find an expression to replace P_1 and P_2. Since the P_{cell} location on the conductivity cell is centered between the two ports for ΔP, we can assume P_1 and P_2 are one half of $\Delta P \pm P_{cell}$ as shown in Equation 2.10 and Equation 2.11 below. Additionally, an expression for mass flow rate and area in terms of the fracture must be substituted.

$$P_1 = P_{cell} + 0.5\Delta P \tag{2.10}$$

$$P_2 = P_{cell} - 0.5\Delta P \tag{2.11}$$

Using values of fracture width, w_f, and sample width, h_f, an expression for area, *A* is shown below.

$$A = w_f h_f \tag{2.12}$$

Mass flow rate can be expressed in terms of volumetric flow rate and fluid density with Equation

$$\dot{M} = q\rho_f \tag{2.13}$$

Combining Equations 2.10, 2.11, 2.13, and 2.12 with Equation 2.9, and rearranging we obtain the equation below.

$$\frac{\left[(P_{cell} + 0.5\Delta P)^2 - (P_{cell} - 0.5\Delta P)^2\right]}{2L}\frac{M_g}{ZRT} = \frac{\mu q \rho_f}{h_f}\frac{1}{w_f k_f} \tag{2.14}$$

Using the definition of fracture conductivity, $C_f = k_f w_f$, and combining with Equation 2.14 below, we obtain the equation used to calculate conductivity for the nitrogen stages.

$$\frac{\left[(P_{cell} + 0.5\Delta P)^2 - (P_{cell} - 0.5\Delta P)^2\right]}{2L}\frac{M_g}{ZRT} = \frac{\mu q \rho_f}{h_f}\frac{1}{C_f} \tag{2.15}$$

Where the three unknown variables P_{cell}, ΔP, and q are measured values during the experiment. Constants h_f and L are known measurements from the conductivity sample. M_g, Z, μ, and ρ_f are known values of nitrogen at the room temperature in which the experiments were conducted. To ensure the ideal gas law withstands, the properties of nitrogen do not change throughout the experiment, the pressure drop was kept below 10% of P_{cell}. R is the universal gas constant.

For Darcy flow through a fracture we plot $\frac{\left[(P_{cell} + 0.5\Delta P)^2 - (P_{cell} - 0.5\Delta P)^2\right]}{2L}\frac{M_g}{ZRT}$ versus $\frac{\mu q \rho_f}{h_f}$ for each of the recorded flow rates and pressures for a given closure stress. To obtain the conductivity value, a linear best fit line is found, and the inverse of the slope gives the conductivity value at each closure stress. While more than four points can be used to calculate conductivity, four points are adequate to give a best fit to obtain conductivity.

To calculate conductivity in the Forcheimer's flow regime, Zhang (2014) presented a

methodology of plotting $\frac{P_{cell}M_g\Delta Ph_f}{ZRTL\mu q\rho_f}$ versus $\frac{q\rho_f}{h_f\mu}$. This method is similar to the Darcy flow method, however the inverse of the y-intercept of this plot provides the calculated fracture conductivity.

2.3.2.2 Water Conductivity Calculation

Conductivity values for the water stage of the experiment were calculated using the Darcy equation for flow. Starting with the general form of the Darcy equation below:

$$-\frac{dp}{dL} = \frac{\mu v}{k_f} \tag{2.16}$$

We rearrange Equation 2.16 such that *dL* is on the right hand side of the equation. Integrating the equation, we have:

$$\Delta P = \frac{\mu v}{k_f} L \tag{2.17}$$

Flow velocity, v is related to both volumetric flow rate and flow area.

$$v = \frac{q}{A} \tag{2.18}$$

Substituting Equation 2.18 into Equation 2.17 yields

$$\Delta P = \frac{\mu q}{k_f A} L \tag{2.19}$$

Using the relationship between area and fracture and sample width, $A = w_f h_f$, we obtain the expression below.

$$\Delta P = \frac{\mu q L}{k_f w_f h_f} \tag{2.20}$$

Substituting the expression for conductivity, $C_f = k_f w_f$, into Equation 2.20 and rear-

ranging we obtain the following.

$$C_f = \frac{\mu q L}{\Delta P h_f} \tag{2.21}$$

Finally, a constant is introduced to allow for laboratory experiment measurements to be used and the final expression to calculate fracture water conductivity is shown in Equation 2.22. Using this conversion factor, μ is in cP, q is in mL/min, ΔL is in in., ΔP is in psi, and h_f is in in.

$$C_f = \frac{\mu q L}{0.1244 \Delta P h_f} \tag{2.22}$$

2.3.3 Methodology of Water Fracture Conductivity Test

The water fracture conductivity test is composed of three unique stages. The first stage uses dry nitrogen as the fluid, and establishes a baseline conductivity for the sample. The second stage, or the damaging stage, flows a reconstituted brine through the fracture. This is called a damaging conductivity test because the water rock interactions effectively change the fracture environment from the nitrogen stage. The third stage uses dry nitrogen again to recover the conductivity. Details of the methodology for each of these three stages follow.

2.3.3.1 Nitrogen Pre-Water

The pre-water nitrogen conductivity test provides a baseline conductivity curve for a given fractured and propped sample. The following steps are taken to complete this stage.

1. Once the sample has cured in the epoxy coating, port openings for inlet, outlet, and pressure gauges are cut. These ports are cut according to the measurements shown in Figure 2.13, cutting a 1/2 inch box around the center of each measurement point.

2. Teflon pipe thread tape is wrapped around the sample as shown in Figure 2.13, and vacuum grease is applied on the entire epoxied surface, except below the port openings.

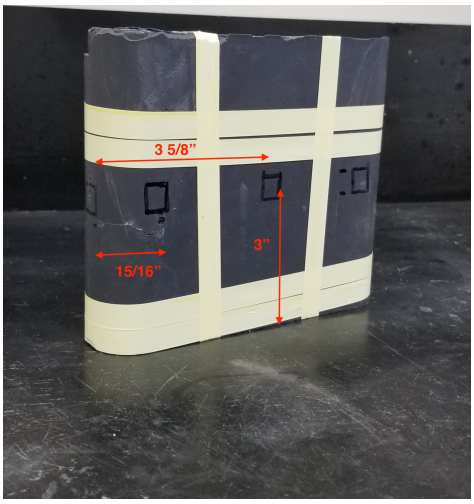

Figure 2.13: Measurements for port openings, and correct wrapping of Teflon tape to aid in sealing sample in conductivity cell.

3. The bottom piston is inserted into the bottom of the conductivity cell until it stops from the spacer plate as shown in Figure 2.14.

4. Sample is loaded into the cell from above until it makes contact with the lower piston. A small rod is inserted through the pressure port opening, and is tapped against the rock surface to achieve a "knocking" sound to ensure communication of the fracture through the pressure ports.

5. Top piston is inserted into the cell, and the endcaps are then bolted on. Figure 2.14 pictures what the complete assembly should look like.

Figure 2.14: Completed conductivity cell assembly with sample placed inside.

6. The assembly is placed under the GCTS piston, such that this is aligned with the top piston of the assembly, and the inlet and outlet lines are attached to the assembly.

7. At this point the GCTS Control program is initiated, and the window view shown in Figure 2.8 is loaded.

8. The cell pressure and differential pressure sensors are calibrated and zeroed, and are then attached to the cell assembly.

9. A new load program is initiated to load the sample to 1000 psi (48 kN) closure stress at a rate of 5.6 kN/min. Upon reaching the target closure stress, the plugs are inserted into both the top and bottom pistons to close the system to leakoff.

10. The system is held at this target stress for at least 40 minutes to account for rock creep and allow the fracture to reach an in-situ condition under that stress.

11. The backpressure valve is closed and nitrogen is flowed into the conductivity cell until the cell pressure reads 35 psi.

12. Flow is initiated through the fracture until a pressure differential of at least 0.2 psi is registered. This flow rate is allowed to reach a constant value before it, cell pressure, and differential pressure values are recorded. These values are used in an Excel sheet to calculate conductivity.

13. Once the first flow point has been measured, the flow is reduced by about 500-1000 mL/min and allowed to reach steady state. The values are then recorded.

14. The previous two steps are repeated until four total measurements at 1000 psi closure stress have been recorded. Nitrogen is then shut off from the system with the back pressure valve open, and a new program is initiated to increase closure stress by an additional 1000 psi.

15. Step 9 to Step 14 are repeated for 2000 psi, 3000 psi, and 4000 psi closure stress respectively.

16. Upon recording the final point at 4000 psi closure stress, the first stage of the water conductivity test has ended and nitrogen is closed off from the system. Load is held constant at 4000 psi for the duration of the experiment.

2.3.3.2 Water Stage

The water stage of the conductivity experiment exposes the fractured rock to a reconstituted brine solution, representing the damaged portion of the test. The line connected to the syringe pump is attached to the four-way fitting such that the entire assembly looks like Figure 2.15. The following steps occur after nitrogen has been closed off from the system, at a constant closure stress of 4000 psi.

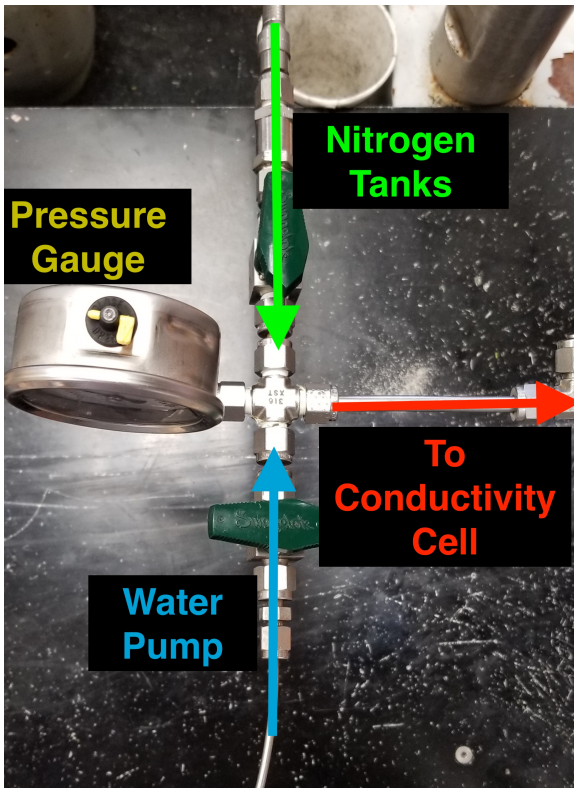

Figure 2.15: Fully assembled line connections for water fracture conductivity test.

1. The valves at the inlet and outlet of the conductivity cell are closed off, sealing the fracture from the system lines.

2. The valves connecting the pump to the system and the bypass valve are opened, and the backpressure valve is closed.

3. Water is pumped through the bypass line at a constant rate of 10 mL/min until the pressure measured at the center of the sample, P_{cell} is built up to 30 psi, at which pumping is paused.

4. Any leaks observed are addressed at this time.

5. In rapid succession, flow is reduced to 2 mL/min and initiated, the backpressure valve

is slowly opened, the bypass valve is closed, and the inlet valve to the conductivity cell is slowly opened to ensure the differential pressure sensor's range is not exceeded.

6. Outlet valve for the conductivity cell is then opened and the backpressure valve is fully opened.

7. Once droplets are observed exiting the effluent line, the inlet and outlet valves are closed and pumping is paused.

8. The pump is refilled until full, at which time flow is switched to the conductivity system and the pressure measured at the pump is slightly higher than cell pressure.

9. Inlet valve followed by outlet valve are opened and the system is allowed to flow until a steady differential pressure, or "steady-state" is achieved.

10. If pump needs additional refills, Step 7 to Step 9 are followed as necessary.

11. Upon reaching steady-state, the pump is shut off, inlet and outlet valves are closed, and the bypass valve is opened.

2.3.3.3 Nitrogen Flow Post-Water

Following the flow of water, the last stage of the water conductivity test is to reintroduce dry nitrogen to the fracture in order to calculate the degree of water impairment. As stated before, this entire stage is conducted at 4000 psi closure stress. This stage is similar to the first nitrogen stage, save for a few key changes.

1. After water is finished, the primary control valve for nitrogen is opened until a pressure of 30 psi is attained.

2. At 30 psi, the valve connecting nitrogen to the system is opened, flushing the bypass line and effluent line of residual water.

3. Flowrate is adjusted using the backpressure valve until a constant rate of 1000 mL/min is reached.

4. The bypass valve is closed, and the inlet valve to the cell is slowly opened such that the range of the differential pressure sensor is not exceeded.

5. Once the inlet valve is fully open, the outlet valve is slowly opened.

6. Nitrogen is allowed to flow through the fracture continuously.

7. Every 40 minutes, Step 9 to Step 14 from the first nitrogen stage are followed to obtain flow and pressure measurements to perform a 4-point conductivity calculation. However, the closure stress will remain constant and flow of nitrogen will be reduced to its initial rate in Step 6.

8. This procedure is repeated every 40 minutes until a constant calculated value of conductivity is achieved, at which point the system is ready for disassembly.

2.3.3.4 Disassembly

After the second stage of nitrogen reaches a steady-state conductivity value, the flow of nitrogen is shut off from the system. The backpressure valve is fully opened while maintaining the differential pressure within its limits, to decrease the pressure in the system to the atmospheric pressure. Once the gas pressure is relieved the lines for inlet, outlet, and pressure sensors can be removed. This is followed by removing the leakoff plugs and the bolts for the inlet and outlet endcaps. At this point the conductivity cell is ready to be relieved of stress, so an unload program is initiated. Finally, the top piston is removed, and the bottom piston followed by the fracture conductivity sample, are removed using a manual vertical hydraulic press. Wooden blocks are used to interface between the sample surface, and the face of the load piston

This procedure is then repeated for each sample tested.

3. RESULTS

This chapter will cover the experimental results for the study of the Meramec mudstone. Results included in this chapter are laser profilometer surface scan of surface roughness, fracture conductivity water test results, XRD mineralogy analysis, and proppant sieve analysis.

3.1 Sample Surface Scan and Roughness Results

This section covers the laser profilometer scan of the fracture surface for each sample. The total, planar flow area for the conductivity cell is 10.81 in^2, but to ensure edge effects do not affect the surface area analysis, the analyzed flat area was reduced to 8.81 in^2 for each sample. Total area of each sample was calculated accounting for changes in topography.

3.1.1 Surface Scan of 0.2 lb/ft^2 Tests

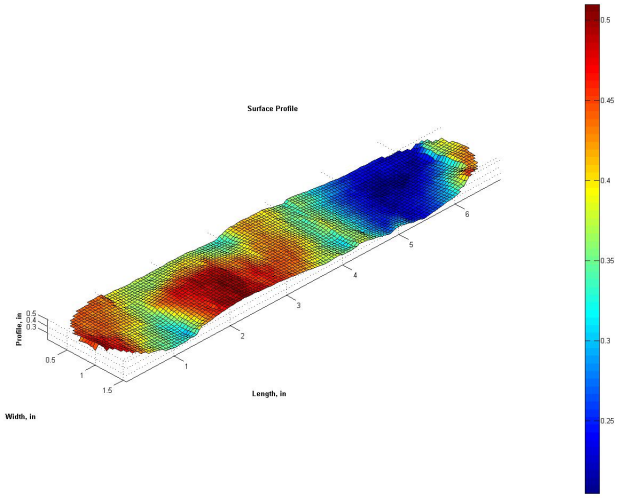

Figure 3.1: Laser profilometer surface scan of 0.2 lb/ft^2 20/40 mesh sample.

Figure 3.1 shows the surface scan of the 0.2 lb/ft^2 20/40 mesh sample. Total surface area of this sample was 9.07 in^2, yielding a difference in area of 0.26 in^2, or a 2.94% difference. The fracture surface roughness for this sample was calculated to be 0.14 in., while the maximum surface height difference, or ΔZ was 0.30 in.

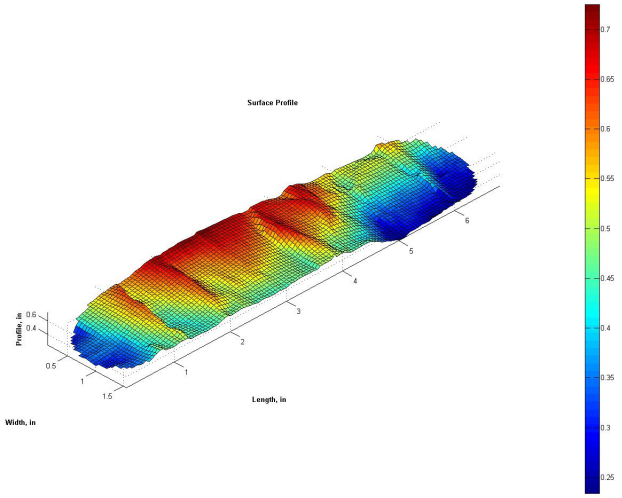

Figure 3.2: Laser profilometer surface scan of 0.2 lb/ft^2 30/50 mesh sample.

Shown in Figure 3.2 is the surface scan of the 0.2 lb/ft^2 30/50 mesh sample. The total surface area of this sample was the largest of the sample set at 9.44 in^2, producing a difference in area of 0.63 in^2, or 7.13%. Additionally, this sample had the largest fracture surface roughness value at 0.20 in., and the largest ΔZ value of 0.49 in. This change in vertical topography is seen in Figure 3.2, where there is a large depression near the inlet, while the port side of the fracture contained a higher ridge.

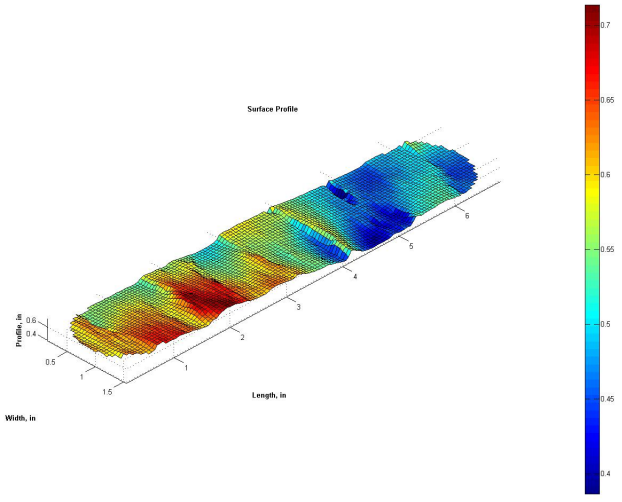

Figure 3.3: Laser profilometer surface scan of 0.2 lb/ft^2 40/70 mesh sample.

Figure 3.3 shows the surface scan of the 0.2 lb/ft^2 40/70 mesh sample. Total surface area of this sample was 9.21 in^2, yielding a difference in area of 0.40 in^2, or a 4.52% difference. The fracture surface roughness for this sample was calculated to be 0.19 in., which was second largest for this sample set. The maximum surface height difference, or ΔZ was 0.33 in, observed in the Figure, showing a slight dip in the fracture surface around 5 inches of length, while the outlet saw slight peaks in surface topography.

3.1.2 Surface Scan of 0.4 lb/ft^2 Tests

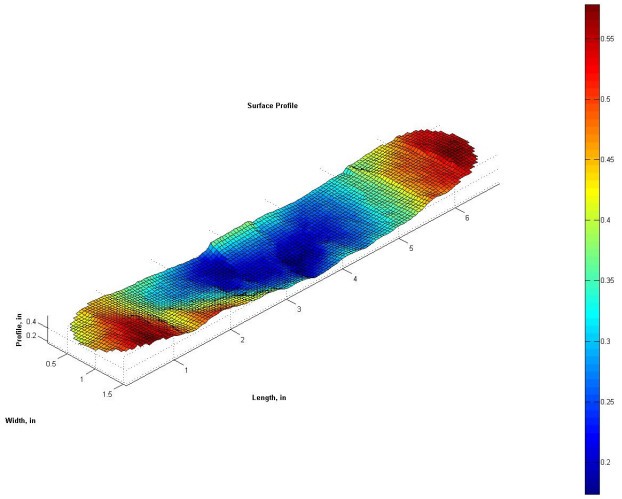

Figure 3.4: Laser profilometer surface scan of 0.4 lb/ft^2 20/40 mesh sample.

Shown in Figure 3.4 is the surface topography scan of the 0.4 lb/ft^2 20/40 mesh sample. The total surface area of this sample was calculated to be 9.11 in^2, producing a surface area difference of 0.30 in^2, or 3.40%. Total fracture surface roughness for this sample was second smallest at 0.16 in., while the ΔZ of this sample was second largest of all samples at 0.40 in. This ΔZ value can be observed in the figure due to the large depression seen in the middle of the sample.

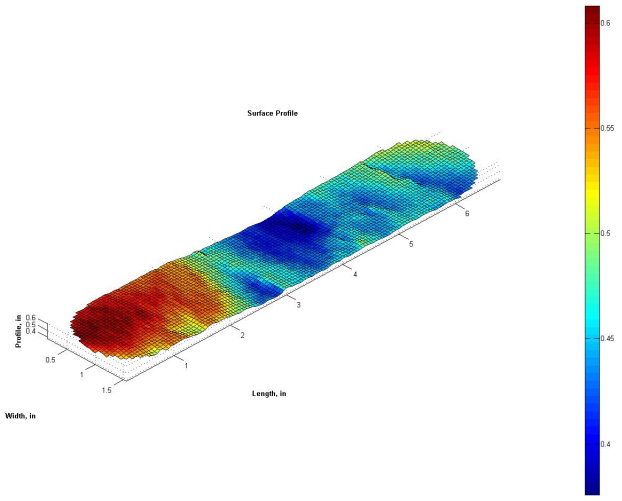

Figure 3.5: Laser profilometer surface scan of 0.4 lb/ft^2 30/50 mesh sample.

Figure 3.5 shows the surface scan of the 0.4 lb/ft^2 30/50 mesh sample. As shown in the figure, the surface profile of this fracture is relatively flat, with a slight depression along the middle. As such total surface area of this sample at 8.95 in^2 was closer to the flat surface area, yielding a difference in area of 0.14 in^2, or a 1.57% difference. The fracture surface roughness for this sample was calculated to be 0.17 in., while the maximum surface height difference, or ΔZ was 0.30 in.

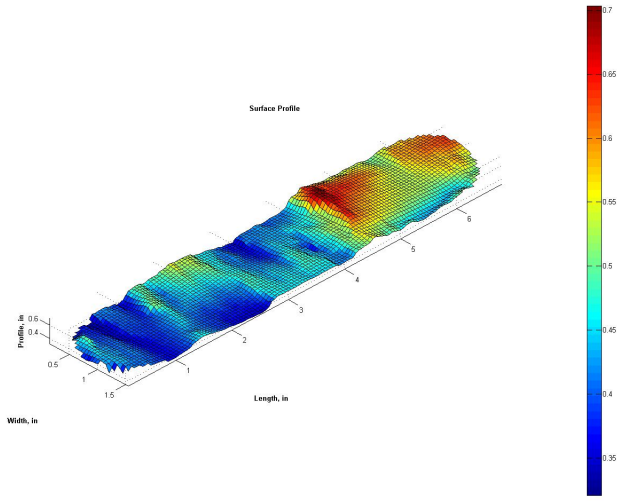

Figure 3.6: Laser profilometer surface scan of 0.4 lb/ft^2 40/70 mesh sample.

Shown in Figure 3.6 is the surface topography scan of the 0.4 lb/ft^2 40/70 mesh sample. The total surface area of this sample was calculated to be 9.22 in^2, producing a surface area difference of 0.41 in^2, or 4.64%, which was second largest among all samples. Total fracture surface roughness for this sample was 0.17 in., while the ΔZ of this sample was 0.38 in. Observing the fracture topography shown in the Figure, a discontinuity in surface elevation can be observed around 4.5 in. sample length, posing a possible pinch point for fracture conductivity tests.

3.2 Fracture Conductivity Water Test

The plots for calculated conductivity as a function of time are shown in the following sections. On the left side y-axis is conductivity in units of mD-ft, and the right side y-axis is closure stress in units of psi. The green dots correspond to the nitrogen stage while the blue line represents the water stage conductivity. The grey dots represent the closure stress at a given time; each dot at 1000 psi, 2000 psi, 3000 psi, and 4000 psi for the first stage have a

corresponding point for conductivity, shown as the green dots.

3.2.1 Conductivity for 0.2 lb/ft^2 Tests

Figure 3.7 shows the water conductivity plot for 0.2 lb/ft^2 20/40 mesh sand. The conductivity curve declined from a starting value of 2330 mD-ft at 1000 psi to 589 mD-ft at 4000 psi. Water was pumped through the fracture for 500 minutes with three total refills until steady state was achieved. The final average conductivity to water was 90 mD-ft. Due to technical difficulties, only one four-point conductivity measurement was observed at 1335 minutes, yielding a calculated gas conductivity of 333 mD-ft. The difference between the pre- and post-water gas conductivities experienced a 43.5% loss in conductivity due to the water damage.

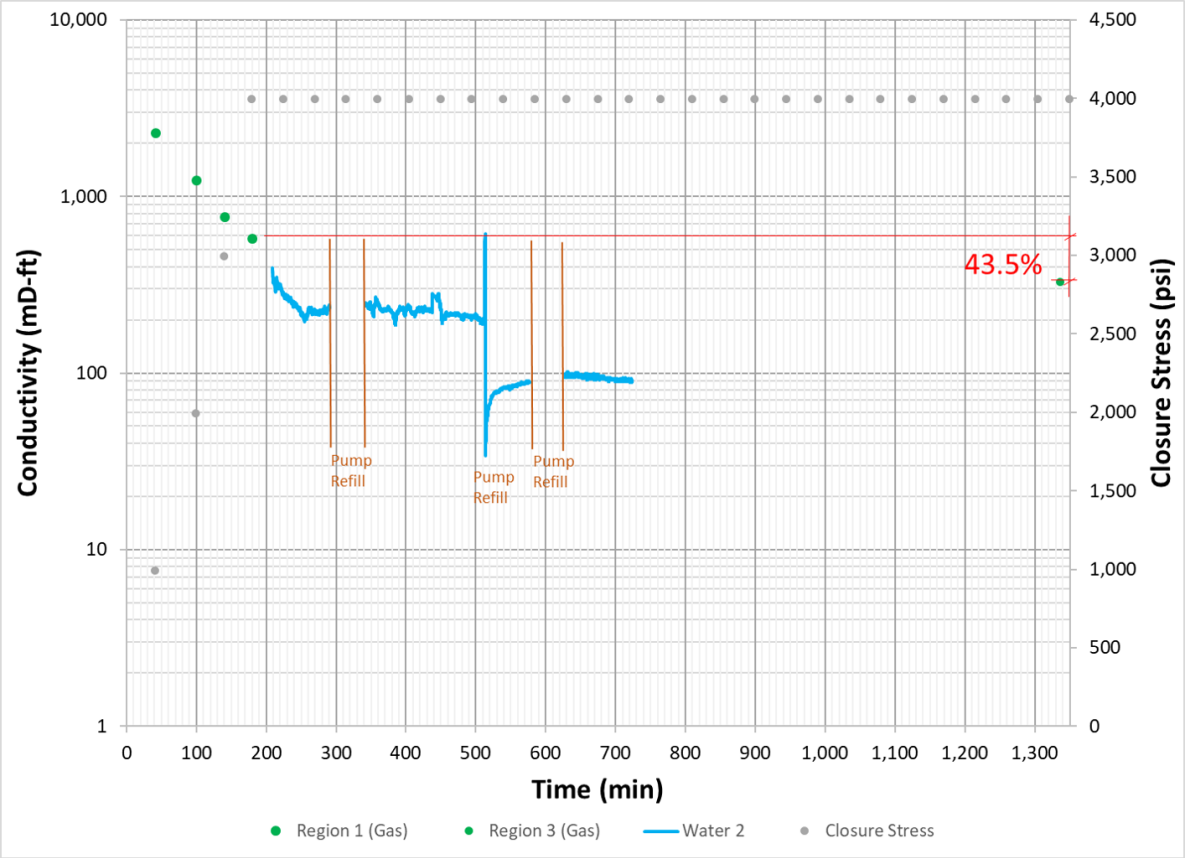

Figure 3.7: Water Conductivity plot for 0.2 lb/ft^2, 20/40 mesh.

Figure 3.8 shows the water conductivity plot for 0.2 lb/ft^2 30/50 mesh sand. Decline in the conductivity from 2000 psi to 4000 psi was observed to be 2012 mD-ft to 1222 mD-ft. The fracture was exposed to water for a duration of 180 minutes with no pump refills needed. It should be noted that slug-like behavior was observed during the water stage, yielding an average calculated conductivity of 374 mD-ft. Five four-point conductivity measurements were needed to safely establish a steady-state post-water conductivity value. The final average conductivity for the post-water nitrogen stage was 931 mD-ft. The difference between pre- and post-water nitrogen conductivities yielded 23.9% unrecoverable conductivity due to water damage.

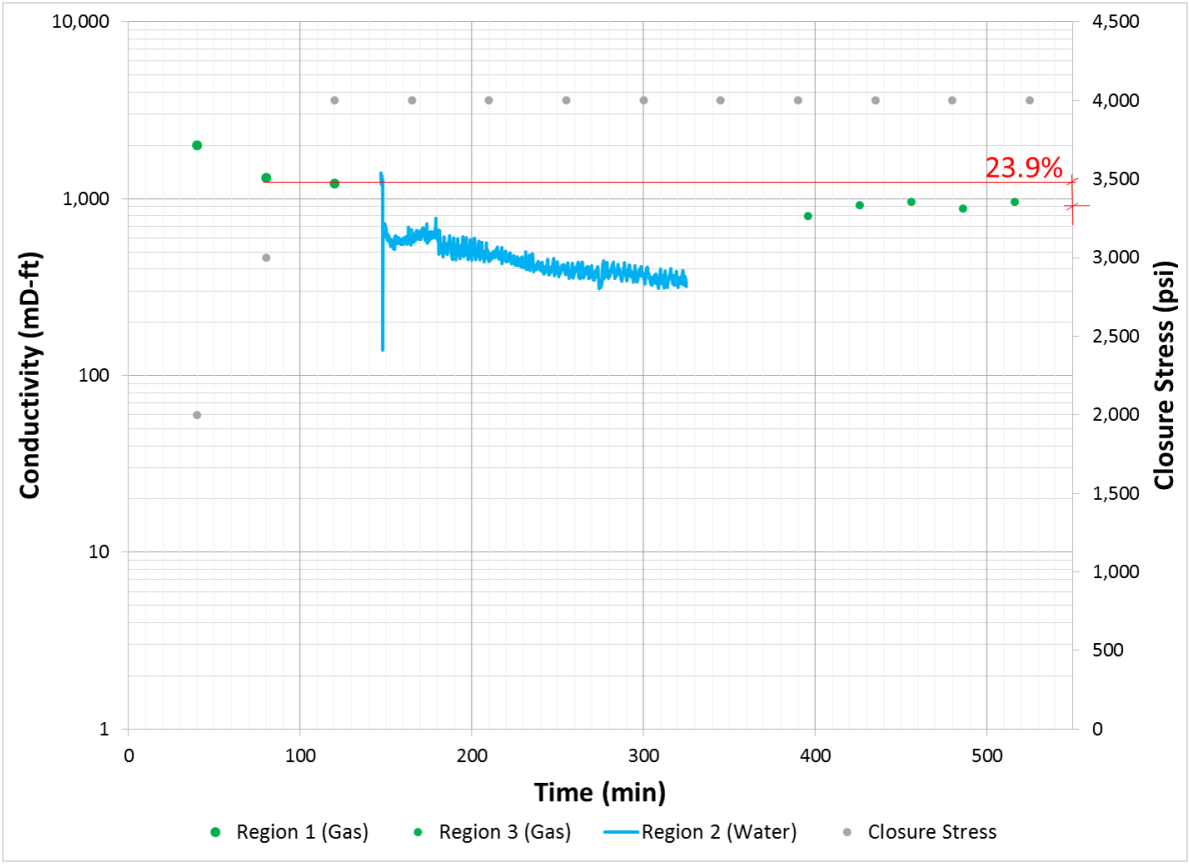

Figure 3.8: Water Conductivity plot for 0.2 lb/ft^2, 30/50 mesh.

The water conductivity test results for the 40/70 mesh sand with 0.2 lb/ft^2 concentration is shown in Figure 3.9. Conductivity at 2000 psi closure stress resulted in a value of 1223 mD-ft and decreased to a value of 610 mD-ft at 4000 psi. Water was introduced to the fracture and was exposed for 210 minutes, without refills. It was noted that occasional slug-like behavior was observed, and a final water conductivity value of 121 mD-ft was calculated. Four four-point conductivity measurements were used to establish a steady-state conductivity value. The average conductivity of these final four points was 280 mD-ft. Unrecoverable conductivity loss from a pre-water value of 610 mD-ft to a post-water conductivity value of 280 mD-ft yielded a 54.2% conductivity loss.

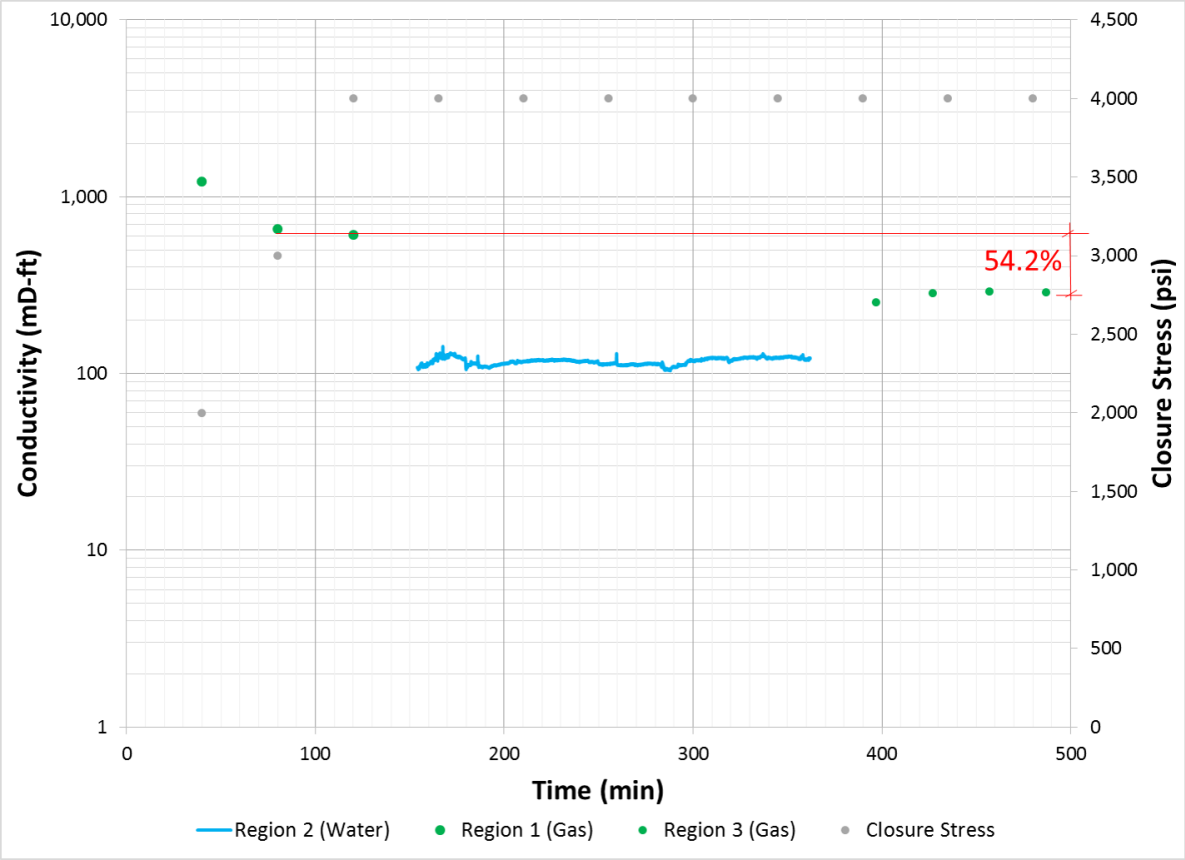

Figure 3.9: Water Conductivity plot for 0.2 lb/ft^2 40/70 mesh.

3.2.2 Conductivity for 0.4 lb/ft^2 Tests

The water conductivity test results for the 0.4 lb/ft^2 20/40 mesh sample are shown in Figure 3.10. Conductivity at 2000 psi closure stress resulted in a value of 1925 mD-ft and decreased to a value of 924 mD-ft at 4000 psi. Water was introduced to the fracture and was exposed for 183 minutes, without refills. It was noted that throughout the water stage slug-like behavior was observed, and a final water conductivity value of 356 mD-ft was calculated. During the post-water gas stage, five four-point conductivity measurements were needed to establish a steady-state conductivity value. The average of these final four point measurements was 773 mD-ft. Unrecoverable conductivity loss from a pre-water value of

924 mD-ft to a post-water conductivity value of 773 mD-ft yielded a 15.6% conductivity loss.

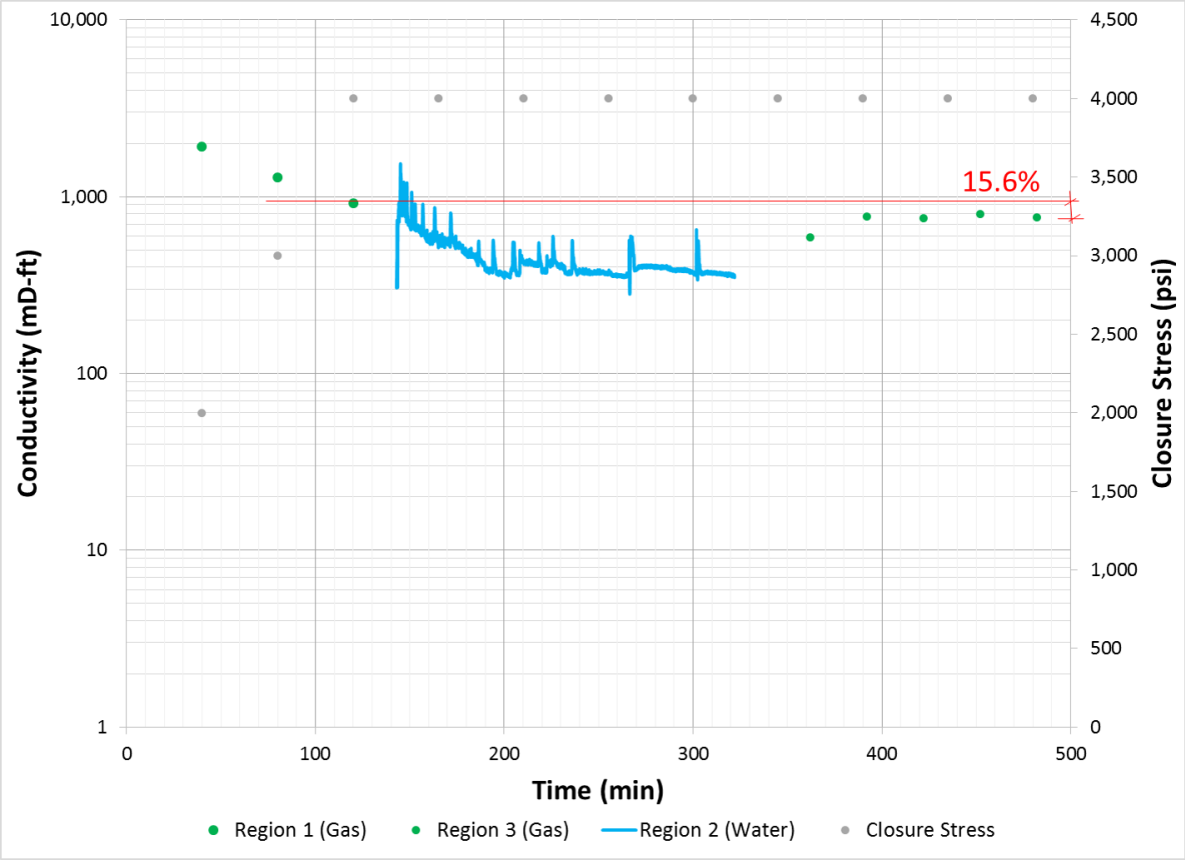

Figure 3.10: Water Conductivity plot for 0.4 lb/ft^2, 20/40 mesh.

Figure 3.11 shows the fracture conductivity plot for 0.4 lb/ft^2 30/50 mesh sand. The conductivity curve declined from a starting value of 1541 mD-ft at 2000 psi to 941 mD-ft at 4000 psi. Water was pumped through the fracture for 426 minutes with two pump refills until steady state was achieved. Throughout the water stage, slug-like flow behavior was observed. The final average conductivity at the end of water flow was 185 mD-ft. A total of four four-point conductivity measurement were needed to achieve steady-state for the final

gas stage, yielding a calculated gas conductivity of 446 mD-ft. The difference between the pre- and post-water gas conductivities of 941 mD-ft and 446 mD-ft respectively, resulting in a 52.6% loss in conductivity due to water exposure.

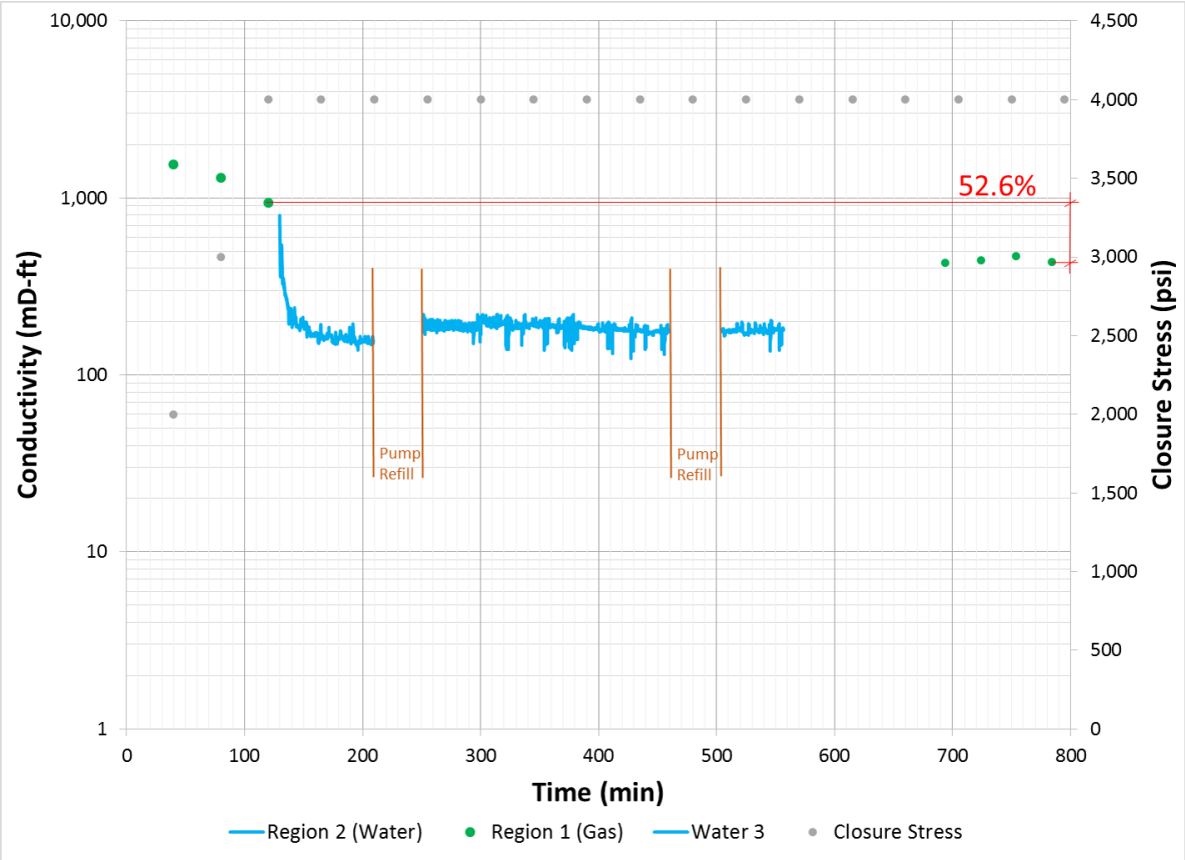

Figure 3.11: Water Conductivity plot for 0.4 lb/ft^2, 30/50 mesh.

Figure 3.12 represents the water conductivity plot for 0.4 lb/ft^2 40/70 mesh sand. Decline in conductivity from 2000 psi to 4000 psi was calculated to be 1938 mD-ft to 513 mD-ft. The fracture was exposed to water for a duration of 329 minutes with one pump refill needed. It should be noted that intermittent slug-like behavior was observed during the water stage, with an average final calculated water conductivity of 135 mD-ft. Five four-

point conductivity measurements were needed to safely establish a steady-state post-water conductivity value. The final average conductivity for the post-water nitrogen stage was 196 mD-ft. The difference between pre- and post-water nitrogen conductivities yielded 61.8% unrecoverable conductivity due to water damage.

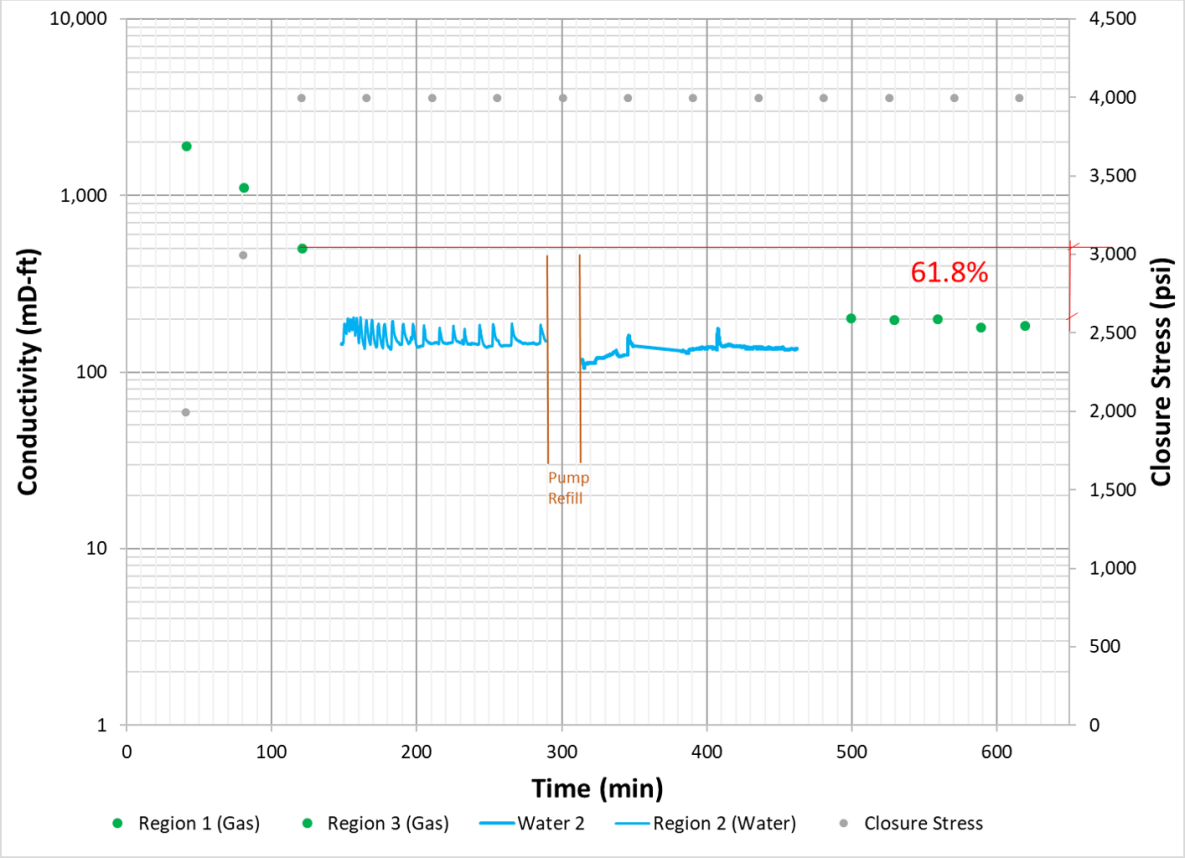

Figure 3.12: Water Conductivity plot for 0.4 lb/ft^2, 40/70 mesh.

3.3 XRD Mineralogy Results

This section introduces the results of the X-Ray Diffraction (XRD) mineralogy analysis. Each rock sample was crushed and sieved to finer than 100 mesh to be analyzed by the Bruker D8 ADVANCE XRD machine. Expected results for this mudstone should include

various clays, limestone, or quartz content. The mineralogy results for the 0.2 lb/ft^2 and 0.4 lb/ft^2 samples are shown below.

The mineralogy results for Sample 1 are shown in Figure 3.13. This sample is located at 9610.2 ft along the depth interval of the obtained core. The predominant mineral is quartz at 53%, followed by feldspar at 17%. Clay minerals found were illite and kaolinite, combined constituted 16% of the core composition. In addition 14% of the sample was composed of calcite.

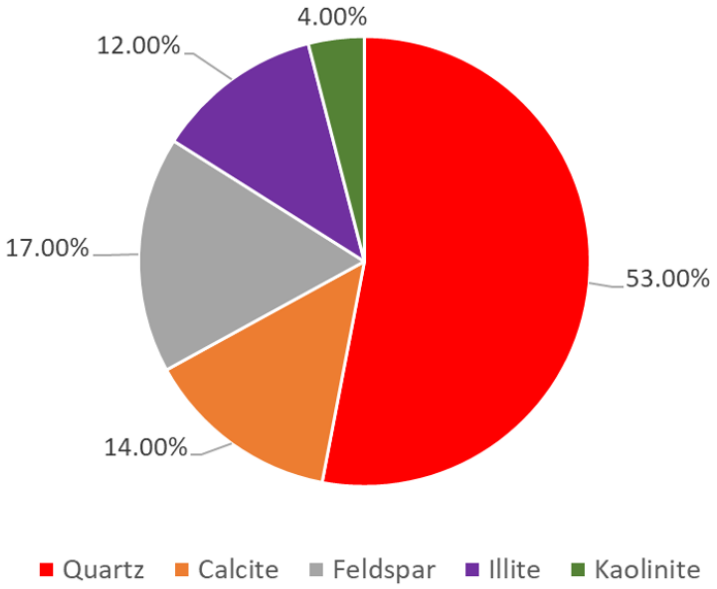

Figure 3.13: Mineralogy results for Sample 1.

Figure 3.14 shows the mineralogy results for Sample 2. The location of this core sample along the depth interval is at 9734.4 ft. The predominant mineral for this core sample is quartz at 50.1%, followed by illite at 29.6%. The total clay content is 32.1% with a 2.5% contribution from kaolinite. Calcite content at this core location is 11.9%, and also contains a trace amount of dolomite at 1.3%.

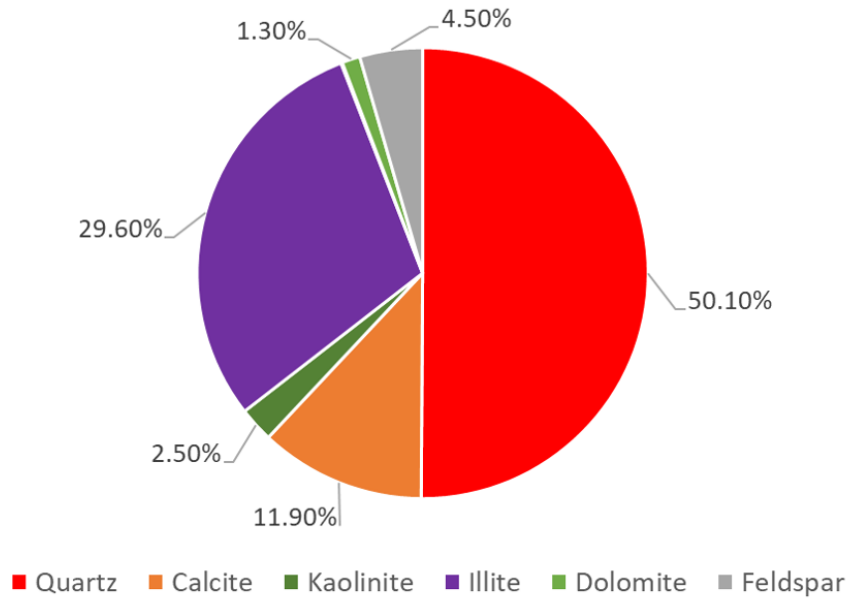

Figure 3.14: Mineralogy results for Sample 2.

Figure 3.15 shows the mineralogy results for the Sample 3. The location of this core sample along the depth interval is at 9730.7 ft. The predominant mineral for this core sample is quartz at 53.4%, followed by illite at 25%. The total clay content is 27.6% with a 2.6% contribution from kaolinite. Calcite content at this core location is 14.1%, and also contains a trace amount of dolomite at 1.1%.

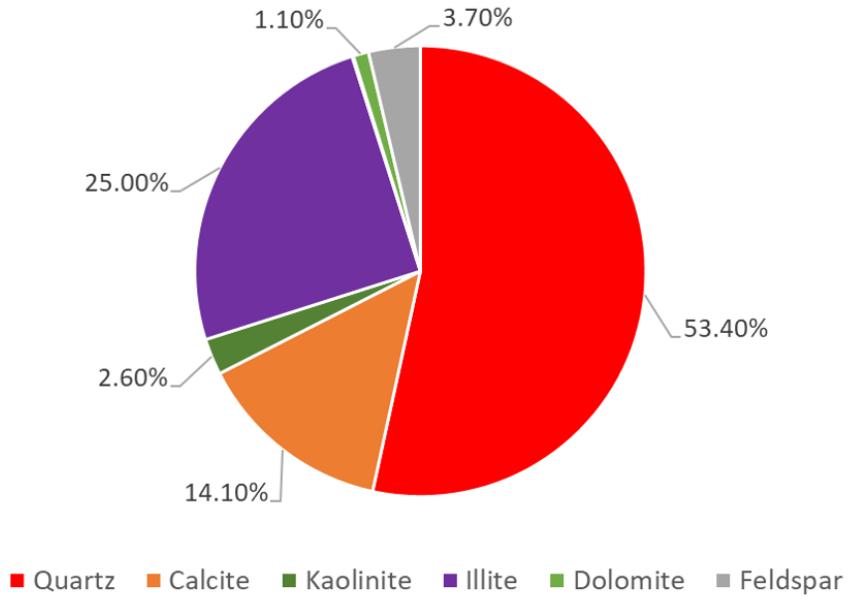

Figure 3.15: Mineralogy results for Sample 3.

Figure 3.16 shows the mineralogy results for Sample 4. The location of this core sample along the depth interval is at 9631.25 ft. The predominant mineral for this core sample is quartz at 48.2%, followed by calcite at 24.5%. Clay minerals are primarily muscovite and kaolinite at 17.7% and 2.6% respectively, yielding a total clay content of 20.3%. Also present at this depth interval is dolomite, contributing 2.6% to the bulk content.

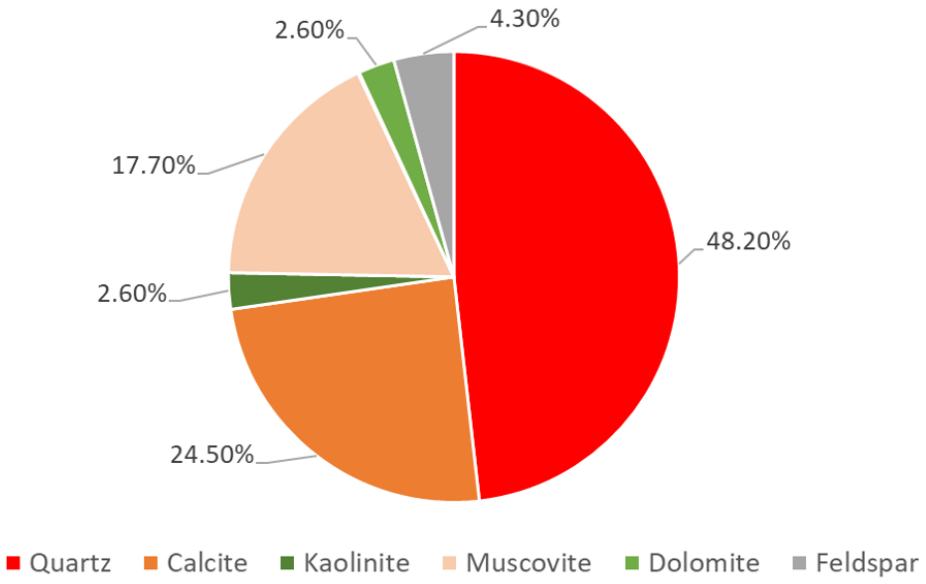

Figure 3.16: Mineralogy results for Sample 4.

The mineralogy results for Sample 5 are shown in Figure 3.17. This sample is located at 9620 ft along the depth interval of the obtained core. The predominant mineral present is quartz at 68.5%, followed by muscovite at 15%. Kaolinite is also present in the core sample at 3.5%. Total clay content at this location in the depth interval is 18.5%. In addition 8.7% of the sample was composed of calcite, and 4.2% feldspar.

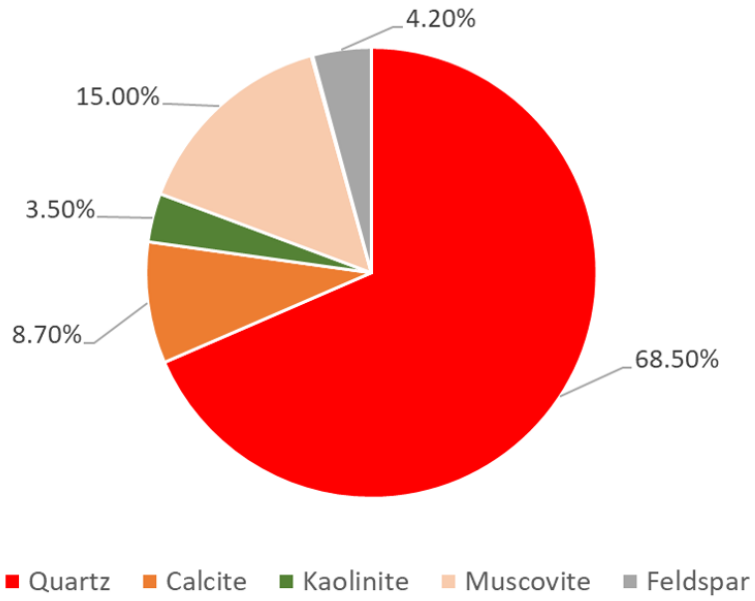

Figure 3.17: Mineralogy results for Sample 5.

Figure 3.18 shows the mineralogy results for Sample 6. The location of this core sample along the depth interval is at 9688.7 ft. The predominant mineral for this core sample is quartz at 36.4%, followed by calcite at 29.6%. The total clay content is 27.5% with a 4.2% contribution from kaolinite and 23.3% composition of muscovite. Also present in this core is dolomite at 3.6%.

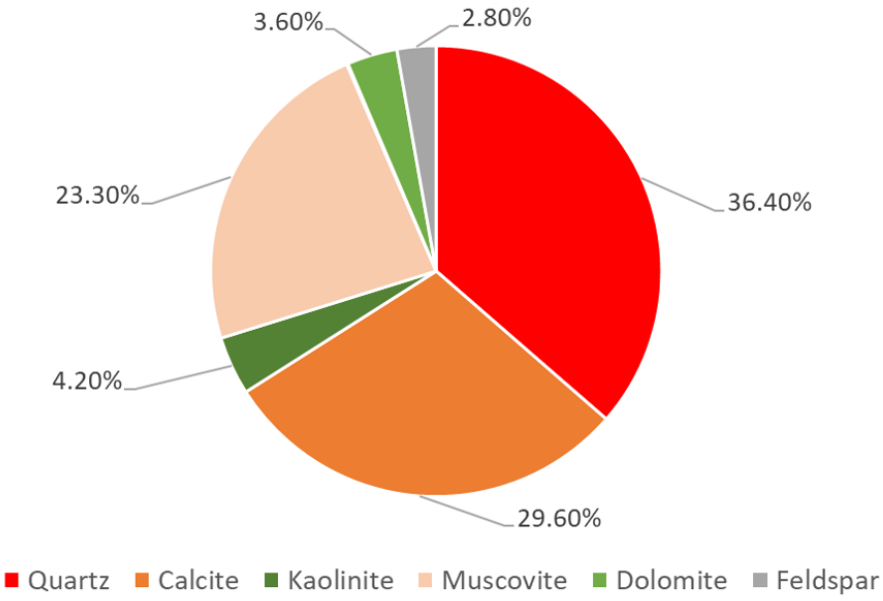

Figure 3.18: Mineralogy results for Sample 6.

3.4 Sieve Analysis Results

This section details the results of a sieve analysis performed on the three HiCrush proppants used. A sieve analysis was done on the bulk proppant before testing, with the results shown in dark blue. Upon completion of the water conductivity experiment the proppant was collected from the fracture surface, dried, and then sieved. The results for the 0.2 lb/ft^2 samples are shown in orange and the 0.4 lb/ft^2 samples are colored gray.

Figure 3.19 shows the results of the sieve analysis for 20/40 mesh HiCrush sand. The pre-test analysis shows a high concentration, 62.82%, of the proppant was captured by the 40 mesh sieve, with the remaining majority captured in the 50 mesh sieve at 29.28%. The sand can be considered fairly well sorted as there is a very small fraction outside the desired mesh size, 1.96% captured at 70 mesh and 1.53% greater than 30 mesh. The results for the 0.2 lb/ft^2 test are shown in orange. It can be seen that a significant amount of proppant crushing has occurred with 48.95% of the proppant size smaller than the 50 mesh sieve. In contrast,

the 0.4 lb/ft^2 test produced less proppant crushing with 26.41% of the proppant size smaller than the 50 mesh sieve.

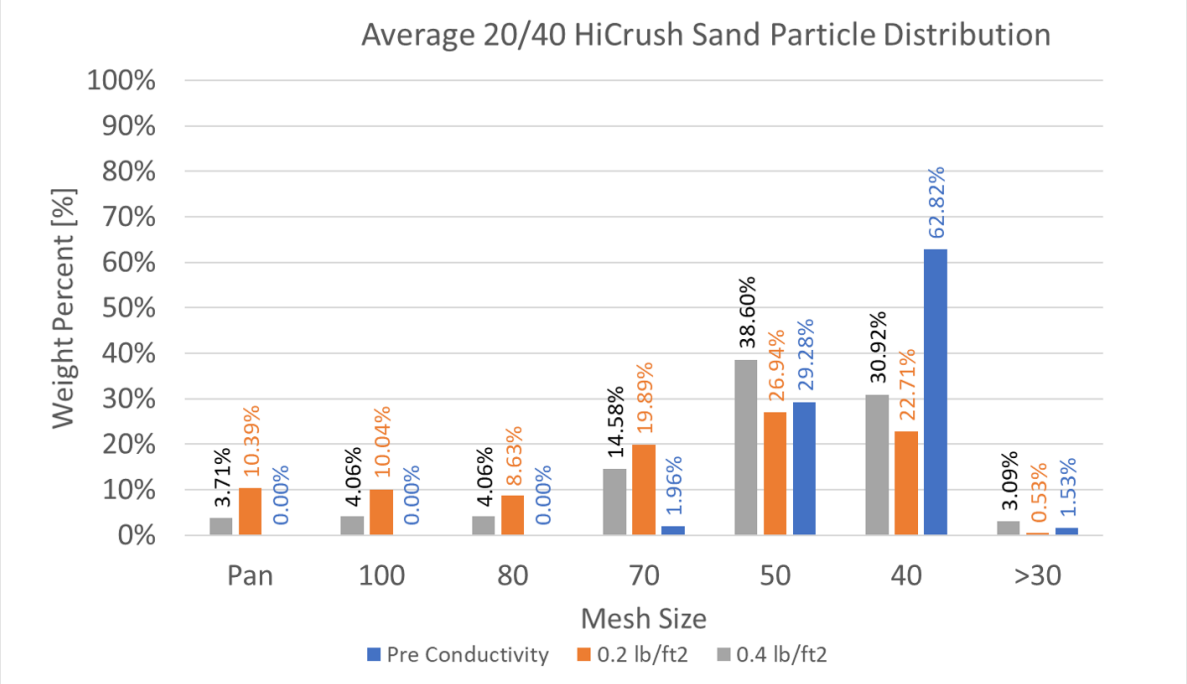

Figure 3.19: Pre- and post-test sieve analysis results for 20/40 mesh sand.

The results for the 30/50 mesh HiCrush sand sieve analysis are presented in Figure 3.20. The pre-test sieve analysis shows results similar to the 20/40 with a relatively well sorted proppant distribution. Just as with the 0.2 lb/ft^2 post test results for 20/40 sand, the 0.2lb/ft^2 30/50 sand exhibited significant proppant crushing. The resulting weight percent smaller than the 50 mesh was 46.19% compared to only 11.84% for the pre-test sieve analysis. Similarly, the 0.4 lb/ft^2 test resulted in less crushing than the 0.2 lb/ft^2 test, but more than the pre-test results. Proppant crushing for the 0.4 lb/ft^2 test produced a 16.58% weight percent of particles smaller than the 50 mesh sieve.

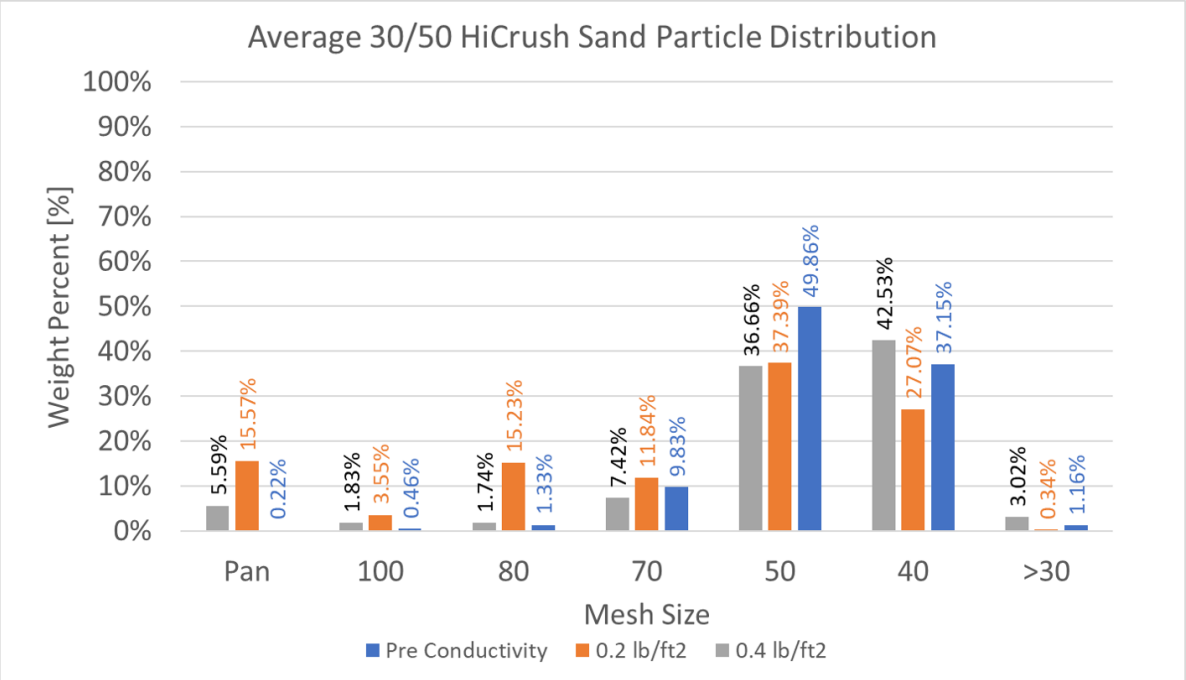

Figure 3.20: Pre- and post-test sieve analysis results for 30/50 mesh sand.

Figure 3.21 shows the results of the sieve analysis for 40/70 mesh HiCrush sand. The pre-test analysis shows a fairly equal concentration of proppant size between the 50 and 70 mesh sieves, 42.37% and 48.86% weight contribution respectively. The sand can be considered fairly well sorted as there is a very small fraction outside the desired mesh size, with 6.46% captured at 80 mesh and 1.56% at 100 mesh. The results for the 0.2 lb/ft^2 test are shown in orange where it can be seen that proppant crushing has occurred, but not as much as the 20/40 and 30/50 mesh tests. The 0.2 lb/ft^2 tests saw 28.58% by weight have a smaller particle size than 70 mesh, compared to 8.11% before the sand was tested. Unlike the previous two proppant types, the 0.4 lb/ft^2 test produced particle sizes with a weight percent closer to the 0.2 lb/ft^2 test with 22% of the proppant size smaller than the 70 mesh sieve.

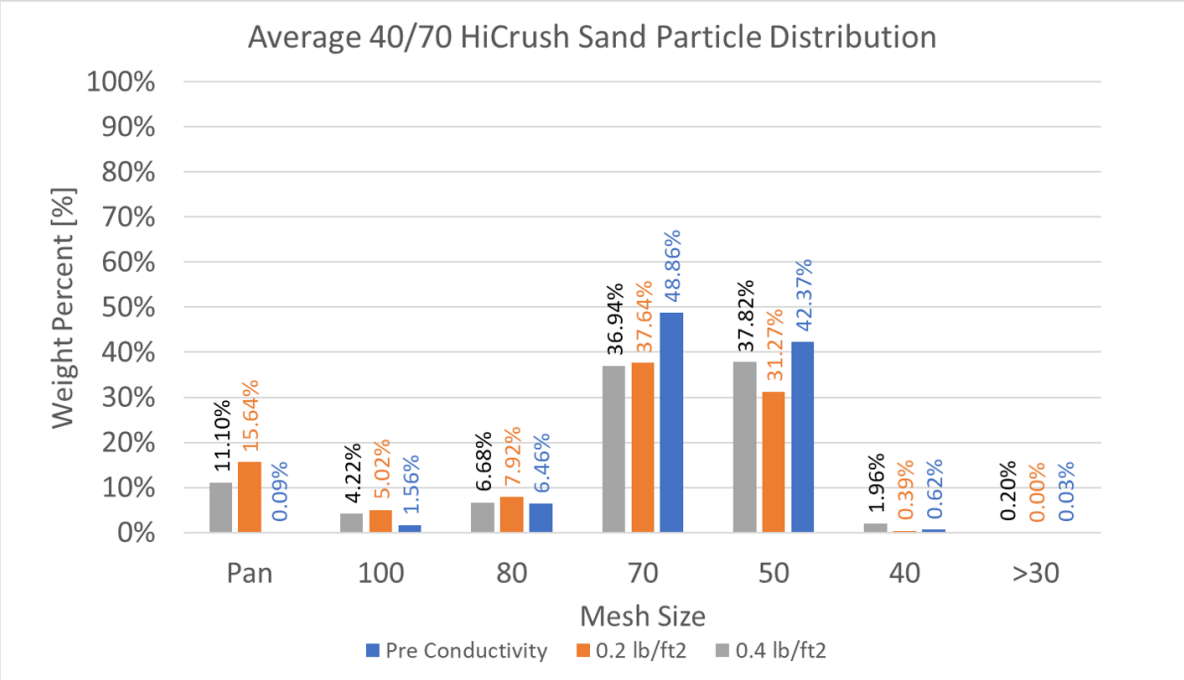

Figure 3.21: Pre- and post-test sieve analysis results for 40/70 mesh sand.

4. DISCUSSION OF RESULTS

4.1 Significance of Surface Roughness and $\triangle$Z Results

Previous studies have shown a significant correlation between surface roughness and fracture conductivity (Enriquez-Tenorio, 2016). As part of the laser profilometer surface scan, values of roughness were calculated using a root-mean-square approach, R_{RMS}. Tabulated values of roughness for the Meramec core used in this study are shown in Table 4.1.

Sample No.	R_{RMS} (in.)
1	0.14
2	0.20
3	0.19
4	0.16
5	0.17
6	0.17

Table 4.1: Tabular values for roughness, R_{RMS} of the six core samples used in experiments.

It has been found that surface roughness primarily affects initial conductivity (Enriquez-Tenorio, 2016). Surface roughness affects initial conductivity as this roughness helps create pathways under low closure stress for the fluid (Fredd et al., 2001). As closure stress increases, mechanisms such as proppant crushing, rock creep, and various other mechanisms dictate conductivity more than surface roughness. Figure 4.1 shows fracture roughness as a function of initial fracture conductivity measured at 1000 psi closure stress. While the data is scattered, there is a discernible upward trend as initial fracture conductivity increases as

fracture surface roughness increases as observed by Enriquez-Tenorio (2016). However due to the scattered nature of the data, more tests need to be conducted to better characterize this behavior for the Meramec formation.

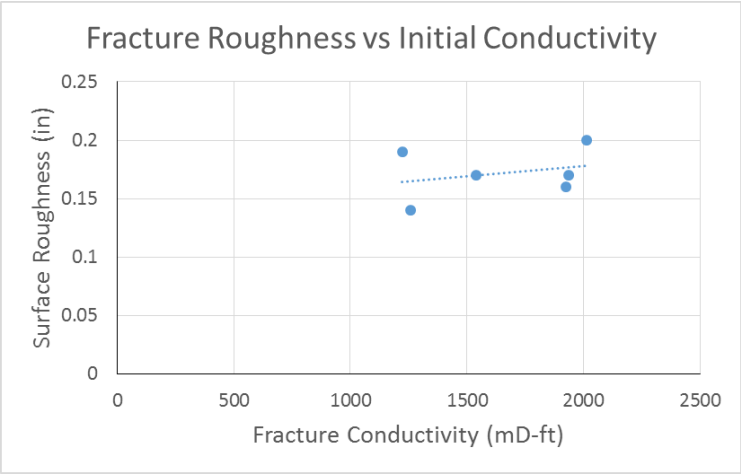

Figure 4.1: Fracture surface roughness versus initial fracture conductivity measurement.

In addition to fracture surface roughness, the maximum vertical change, ΔZ, along the sample surface was also calculated. While previous studies have shown ΔZ to affect loss in conductivity (Zhang, 2014), that behavior was not observed for these core samples. This can be attributed to the surface topography of the samples tested. While Zhang (2014) observed ΔZ to negatively affect recovered conductivity after brine exposure, this was primarily due to the nature of the fractured surface. The samples used for that study contained jagged changes in topography, effectively resulting in pinch points. As observed in the figures from Section III, the samples used in this study did not contain jagged pinch points, but instead the values of ΔZ were a result of gradual inclinations along the surface. Instead, Figure 4.2 investigates the effect of ΔZ versus initial fracture conductivity at 1000 psi.

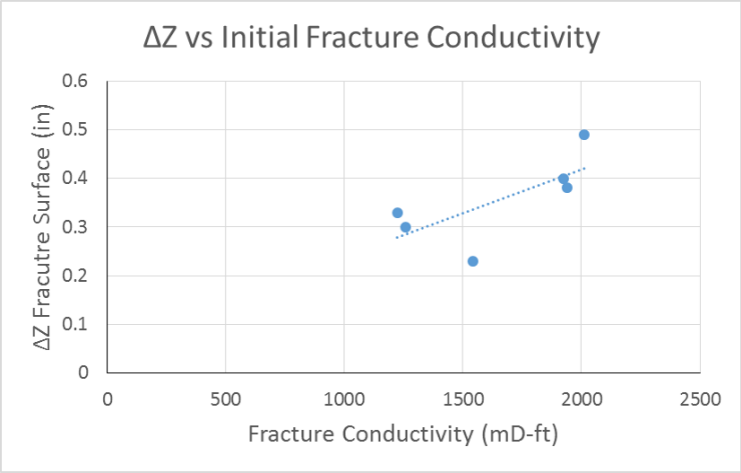

Figure 4.2: ΔZ of fracture surface versus initial fracture conductivity measurement.

As shown in Figure 4.2, there is a proportional trend between ΔZ and initial fracture conductivity. One explanation for this behavior can be derived from a finding by Zhang (2014), where it was found that variations in topography along the fracture surface lead to displacement and concentration of proppant in lower areas of the fracture. Observing the surface of the tested samples, the gradual slopes provide potential for the round sand proppant to become displaced to areas of lower topography. These accumulations of proppant effectively increase the layers of proppant seen in the fracture and increase fracture width under low closure stress. This increase in fracture width due to proppant displacement can lead to higher conductivity as ΔZ.

4.2 Channeling of Proppant

An interesting phenomenon was observed while conducting these water fracture conductivity experiments. With the smaller mesh proppants, and particularly high concentrations (0.4 lb/ft^2), channeling was observed at low closure stress. Figure 4.3a illustrates the correct weight of proppant, spread evenly over the fracture surface, and Figure 4.3b shows channeling phenomenon on a 0.4 lb/ft^2 sample of 40/70 mesh sand.

(a)

(b)

Figure 4.3: 4.3a illustrates the even dispersion of proppant over the fracture face before testing. 4.3b shows the flow pathway formed by proppant channeling at 1000 psi closure stress.

As we can observe from this sample, there are three "pillars" of contact where identifiable proppant crushing has occurred. These pillars in theory carry more load from the closure stress, allowing the unconfined sand grains to mobilize once nitrogen flows through the fracture. This created highway resulted in an abnormally large fracture conductivity value of 4,785 mD-ft at 1000 psi closure stress.

These self-channeling results are consistent with findings by Guerra et al. (2017a), who observed this behavior using Eagle Ford shale conductivity samples shown in Figure 4.4. It was concluded from that study that low proppant concentrations with 100 mesh proppant can exhibit self channeling along with higher concentrations of proppant. Additionally the channeling stems from unsmooth fracture surfaces or variations in proppant concentration due to surface topography. In reality, channeling provides much higher conductivity to benefit production from fracturing. This channeling in the lab experimental conditions is more

likely an artifact because the closure stress is gradually increased. To prevent this effect from occurring, it is recommended starting the experiment at a higher closure stress, hence most of the experiments conducted in this study begin at 2000 psi closure stress.

Figure 4.4: Left image is initial proppant loading of sample, followed by channeling effect seen in picture on right. Reprinted from Guerra et al. (2017a).

4.3 Proppant Crushing

Proppant crushing has been found to reduce conductivity through fractures primarily through fines plugging. These smaller particles are more susceptible to fines migration when fluid is flowed through the fracture, where they can plug the pore space in the surrounding proppant, reducing proppant pack permeability. As shown in Figures 3.19, 3.20, and 3.21, the experiments tested in this study experienced varying degrees of proppant crushing. In this section, the degree of crushing will be investigated, and its effect on dry gas conductivity values.

To quantify the degree of proppant crushing, the following analysis technique will be used. Proppant crushing by weight will be quantified based upon the smallest mesh size for a given proppant. For example, with 20/40 mesh sand, the proppant that is caught in sieves smaller than 40 mesh will be categorized as part of the "crushed" proppant, and this is done for pre-test, post-0.2 lb/ft^2 test, and post-0.4 lb/ft^2 test sieve analyses. These results are tabulated in Table 4.2 below.

Mesh Size	Pre-Test	0.2 lb/ft^2	0.4 lb/ft^2
20/40	31%	76%	65%
30/50	12%	46%	17%
40/70	8%	29%	22%

Table 4.2: Degree of proppant crushing for each mesh size.

It can be shown that post-test, there is significant evidence of proppant crushing. It is noted that the 0.2 lb/ft^2 samples experienced a higher degree of proppant crushing than the 0.4 lb/ft^2 samples. Additionally, for the 0.2 lb/ft^2 samples, the larger the mesh size, the higher the degree of proppant crushing. According to Zhang (2014), this can be explained in terms of neighboring particles for a grain of proppant. The higher the concentration, the more contact a sand grain has to distribute the encountered stress. The disparity between proppant concentrations can be seen due to double the sand found in the fracture. As for the disparity between mesh sizes for the 0.2 lb/ft^2 samples, the same weight of sand is used, so the larger mesh size will have less grains present in the fracture, leading to less neighbors in contact to distribute the closure stress.

Figure 4.5 shows a plot of degree of proppant crushing based on the data in Table 4.2 versus decline in the first gas stage conductivity, the difference between the conductivity at the first closure stress and the final point at 4000 psi closure stress. From this figure, there is a correlation between degree of proppant crushing and loss in conductivity between closure stresses. The point highlighted in orange has been omitted from this best fit analysis as an outlier of the trend. For this particular point, the sample for 0.4 lb/ft^2 of 40/70 sand, the weight of recovered sand post-test was 1.22 g less than the initial proppant load. While there was no evidence of channeling, because this particular mesh size exhibited channeling effects as discussed in the previous section, it is believed that this is the result of fines migration.

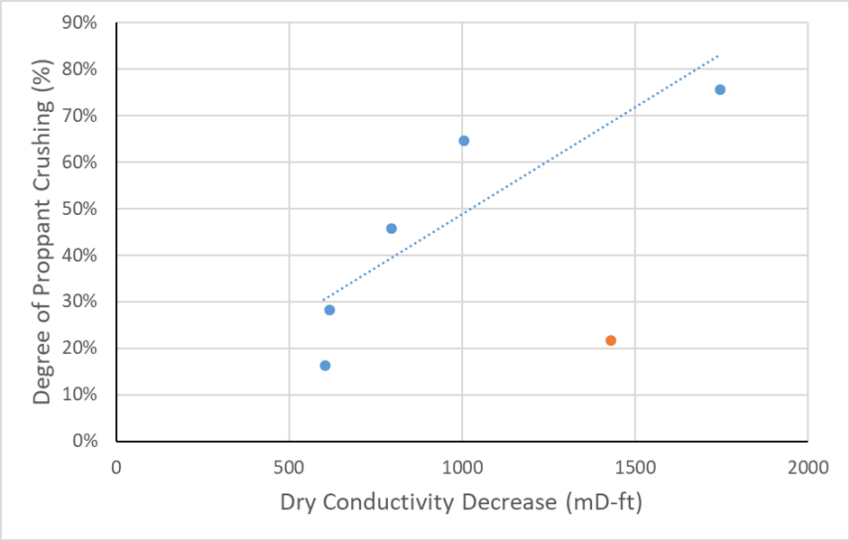

Figure 4.5: Degree of proppant crushing versus decline in conductivity for first gas stage.

4.4 Impact of Repeated Sample Use

Throughout the water fracture conductivity study of the Meramec formation, some samples needed to be reused due to complications during testing, providing an opportunity to analyze the hysteresis effect of cyclic loading and its impact on fracture conductivity results. Due to the limited supply of downhole cores, some cores were tested more than once during this study. Macroscopic degradation of the core samples was not observed during this study, although that does not rule out the possibility of degradation on a micro-level. Figures 4.6, 4.7, and 4.8 show the plots of fracture conductivity versus time for the samples in question. The blue data points in these plots represent the conductivity curve of the first test using each sample, while the orange data points represent the conductivity decline curve of the final, successful water fracture conductivity test.

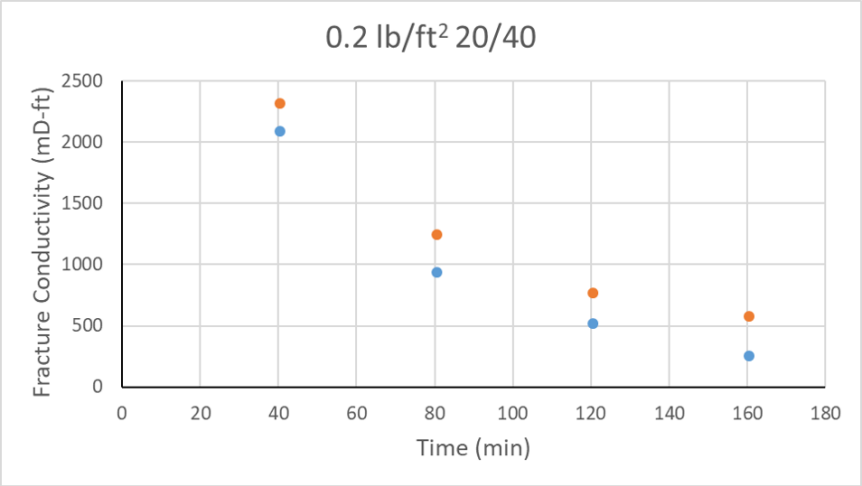

Figure 4.6: Fracture conductivity reuse plot for 0.2 lb/ft^2 20/40 mesh sand.

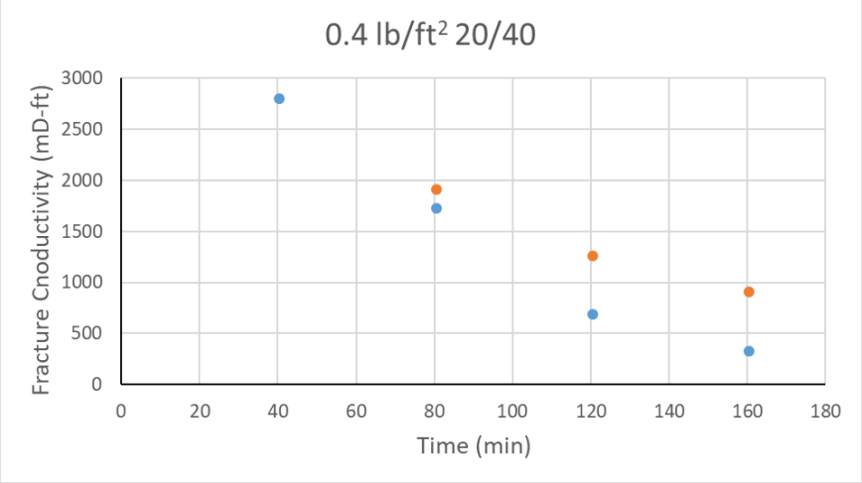

Figure 4.7: Fracture conductivity repeated test plot for 0.4 lb/ft^2 20/40 mesh sand.

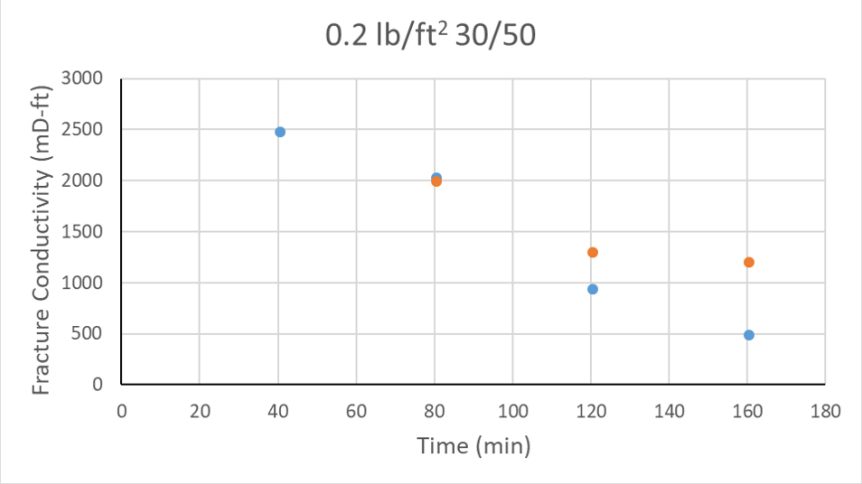

Figure 4.8: Fracture conductivity reuse plot for 0.2 lb/ft^2 30/50 mesh sand.

It was observed across all three samples that the final conductivities were larger than the initial fracture conductivity attempt, with final conductivity values ranging from 31 mD-ft to 718 mD-ft higher than initial values. While it would be expected that damage to the fractured sample from repeated loading would be detrimental to the fracture conductivity values, it was observed that the three reused samples produced recovered fracture conductivity values much higher than the unused samples. Table 4.3 shows the loss in conductivity after water damage for each of the six core samples, with the reused samples in bold and an asterisk.

Sample No.	Unrecoverable Loss in Conductivity
1*	**43.5%**
2*	**23.9%**
3	54.2%
4*	**15.6%**
5	52.6%
6	61.8%

Table 4.3: Table of percent unrecoverable loss in conductivity for each core sample.

This disparity between the reused and one-time test core samples indicates damage to due to water exposure has less of an impact for the reused samples. It was observed that after core samples were cleaned of proppant, sand particles remained trapped on the fracture surface, shown by the red circle in Figure 4.9.

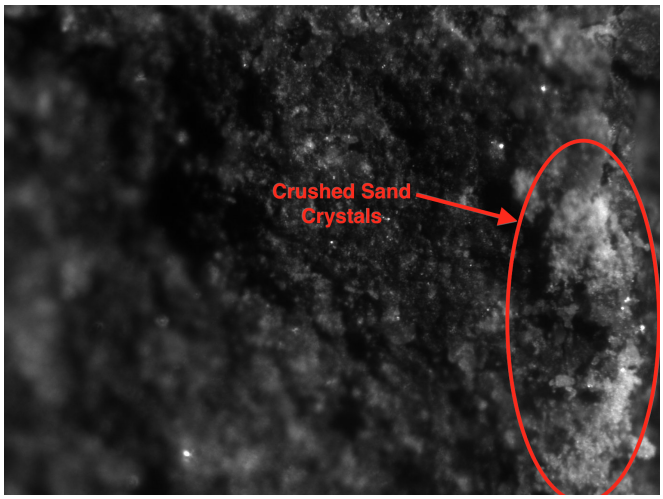

Figure 4.9: Microscope image of fracture surface post-test. Note the embedded sand crystals on the right side of the image.

Figure 4.9 shows the fracture surface under a 2.5x objective microscope lens. It is noticed along the right-hand side of the image there are microscopic sand crystals present on the fracture surface. Despite cleaning of the fracture surface after each test, these crushed sand crystals still remain on the surface, filling the voids of the roughness of the fracture. Figure 4.10 shows the entire fracture surface both top and bottom, with the surface notably whiter in color compared to the freshly fractured sample seen in Figure 2.2.

Figure 4.10: Fracture surface top and bottom, note the white coloration of the fracture surface due to sand crystals adhered to rock after sample cleaning.

The crushed sand coating the fracture surface is believed to cause both the conductivity increase observed in the dry nitrogen conductivity tests, and the lower values of unrecoverable conductivity loss for the water damage tests. This trapped sand effectively increases

the proppant concentration tested, lending itself to increase the effective fracture width. The increase in fracture width would account for the increased dry nitrogen conductivity values observed in Figures 4.6, 4.7, and 4.8. It is also believed that the crushed sand particles reduce the exposed fracture surface area encountering the brine solution. As it was observed in Table 4.3, the reused core samples resulted in lower losses in conductivity. This is due to the crushed sand clogging the fracture surface, effectively reducing the effects of surface softening, among other damage mechanisms due to water-rock interactions.

4.5 Mineralogy and Brittleness in Shales

Mineralogy and its effect on water fracture conductivity results have been heavily investigated. It is known that clay content affects fracture conductivity after exposure to water through surface softening, increased proppant embedment, and release of clay precipitates into the proppant pack are the phenomena that are encountered with water-rock interactions. One of the goals of this study is to contribute to the fracture conductivity database, and compare the Meramec formation and the effect of a reconstituted brine on its loss in conductivity to other tested formations.

The results of the XRD analysis on the six Meramec downhole core tested are summarized in Table 4.4. Comparatively, the results for the Barnett Shale as reported by Zhang (2014), and mineralogy composition of five Eagle Ford shale subunits, A through E, and Marcellus shale outcrops, Elimsport and Allenwood, as reported by Guerra et al. (2017b) are also represented in Table 4.4.

Sample	Quartz	Calcite	Clay	Carbonate	Other
Meramec 1	53.00%	14.00%	16.00%	-	17%
Meramec 2	50.10%	11.90%	32.10%	1.30%	5.90%
Meramec 3	53.40%	14.10%	27.60%	1.10%	4.90%
Meramec 4	48.20%	24.50%	20.30%	2.60%	7.00%
Meramec 5	68.50%	8.70%	18.50%	-	4.30%
Meramec 6	36.40%	29.60%	27.50%	3.60%	6.50%
Barnett	33.00%	-	55.00%	3.00%	10.00%
EF A	7.37%	85.07%	3.46%	3.41%	2.42%
EF B1	11.41%	82.69%	4.40%	0.81%	0.71%
EF B2	25.55%	56.65%	13.46%	2.38%	1.97%
EF B3	28.98%	55.67%	6.45%	3.43%	2.03%
EF C	10.78%	76.75%	10.09%	1.47%	0.93%
EF D	2.42%	93.71%	2.71%	1.01%	0.56%
EF E	3.95%	90.49%	2.56%	2.40%	0.70%
Elimsport	56.00%	4.00%	28.00%	1.40%	9.50%
Allenwood	46.00%	17.00%	25.00%	1.40%	10.20%

Table 4.4: Summarized results for mineralogy analysis of Meramec, Barnett, Eagle Ford, and Marcellus Shales from lab data.

As shown by Table 4.4, there are significant mineralogical differences between the three formations and the Meramec formation. Contrasting clay composition, the Barnett shale had an average clay content of 55%, while the Eagle Ford had a maximum of 13.5%. By comparison, the Meramec on average falls between these two formations with a clay composition similar to the Marcellus; 23.7% and 26.5% respectively. The Meramec also has similari-

ties with the Marcellus formation in quartz content. The average quartz composition for the Meramec was 51.6%, while the Marcellus had 51% quartz on average. This is a stark contrast to the Barnett which had only 33% quartz, and the Eagle Ford that was predominantly composed of calcite.

Additionally, we can draw a correlation between the mineralogical content of these formations and the resulting unrecoverable loss in conductivity after water exposure. Similar to the clay content results, the loss in conductivity due to water follows the same trend. The Barnett Shale had the highest clay content at 55%, and it also had the largest loss in conductivity ranging from 80 to 97% loss in fracture conductivity as reported by Zhang (2014). The Marcellus had an average clay content of 26.5%, and it had an average loss in conductivity of 42.5% as reported by Guerra et al. (2017b). The Meramec core tested contained an average clay content of 23.7%, and average unrecoverable loss in fracture conductivity was found to be 41.9%. Lastly, Guerra et al. (2017b) reported unrecoverable loss in conductivity spanning the five Eagle Ford subunits to be 4.2% up to 24.8%, with a maximum clay content of 13.5%. Characterization of the Meramec formation has shown strong similarities to the Marcellus with regards to clay content and resulting loss in conductivity. Figure 4.11 illustrates the Meramec cores tested, the bright green triangles, versus previously tested formations; the Barnett, Eagle Ford, and Marcellus Shales based upon their respective clay content and loss in conductivity. The Meramec samples tested performed similar to the Marcellus outcrop samples, and these cores follow the trend established by the previously tested formation conductivity tests.

Using the mineralogy data, the brittleness index (BI) of the formation can be calculated. While there are a variety of brittleness indices to choose from, almost all concur that brittleness is dictated by quartz content. Enriquez-Tenorio (2016) reported brittleness index results for the Eagle Ford Shale using the Wang and Gale index, shown in Table 4.5.

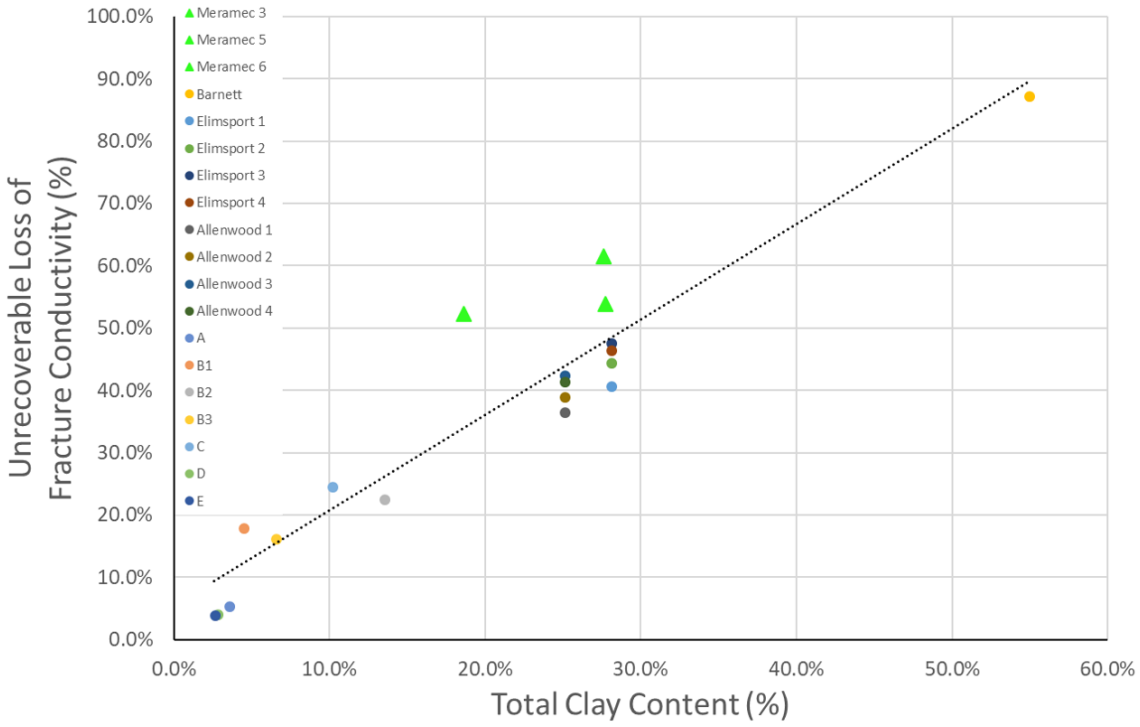

Figure 4.11: Comparison between Meramec core samples and previous studies on the Barnett, Eagle Ford, and Marcellus Shales.

Facies	BI_{Mi}
EA_X	0.11
EB_X	0.19
EB_Z	0.19
EC_X	0.12
ED_X	0.03
EE_X	0.06

Table 4.5: Wang and Gale BI results for Eagle Ford Shale. Reprinted from Enriquez-Tenorio (2016).

The Wang and Gale index specifies that quartz and dolomite content drive the brittleness of the rock, as discussed in Chapter 1. Using this method, the BI results for the Meramec samples are shown in Table 4.6.

Sample No.	BI_{Mi}
1	0.768
2	0.609
3	0.664
4	0.714
5	0.787
6	0.593

Table 4.6: Wang and Gale Brittleness Index values for Meramec core samples.

Comparing the Meramec results to the Eagle Ford brittleness it appears that the Meramec is extremely brittle. However, one of the shortcomings of the Wang and Gale BI is that it does not account for calcite composition, which has been known to have a large impact on increasing brittleness (Kias et al., 2015). One BI that does account for calcite is the Kias

brittleness index. Since the Eagle Ford mineralogy was reported to predominantly contain calcite, the Meramec formation would closely resemble the brittleness of the Eagle Ford on a mineralogical basis using the Kias Index. Brittleness values for Meramec samples using the Jarvie and Kias Brittleness Indices are shown in Appendix A.

4.6 Predicting Conductivity Due to Water Impairment

An important aspect of this study was to quantify how water impairment in the Meramec formation compares to other major oil and gas producing shale reservoirs. Zhang et al. (2015) proposed a method to predict recoverable conductivity in the Barnett shale across different proppant concentrations. Using a modified Berg model to calculate conductivity, he was able to predict undamaged conductivity at low proppant concentrations. Through this model he proposed an exponential equation equating recoverable conductivity as a function of calculated undamaged conductivity. The development of this model proves useful as it is an inherent function of proppant and formation properties, allowing for predicted recoverable conductivity values without the need for a full scale water conductivity test.

Figure 4.12 shows the results of Zhang's test that lead to the formation of the exponential correlation. He concluded that the lower two points were due to proppant disparities along the fracture surface from slopes in the fracture. These areas were found to be susceptible to water damage, resulting in decreased fracture conductivity. The equation for these data points is shown in Equation 4.1 where $C_{f,recovered}$ is recovered conductivity, and $k_f w_f$ is the undamaged conductivity (Zhang et al., 2015).

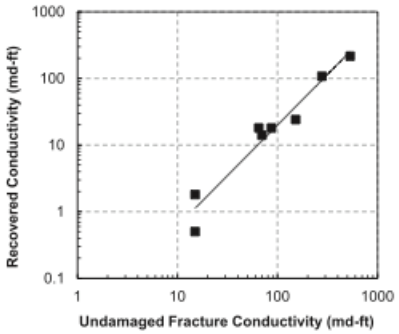

Figure 4.12: Trend for recoverable conductivity versus undamaged conductivity. Reprinted from Zhang et al. (2015)

$$C_{f,recovered} = 0.0185(k_f w_f)^{1.5168} \tag{4.1}$$

Water conductivity values were extracted from Guerra et al. (2017c) and used to create power law plots for the Eagle Ford and Marcellus Formations, where these plots are also characterized in Guerra (2018). Utilizing the approach suggested by Zhang, correlations for the Marcellus and Eagle Ford shale formations are shown in Figure 4.13 and Figure 4.14.

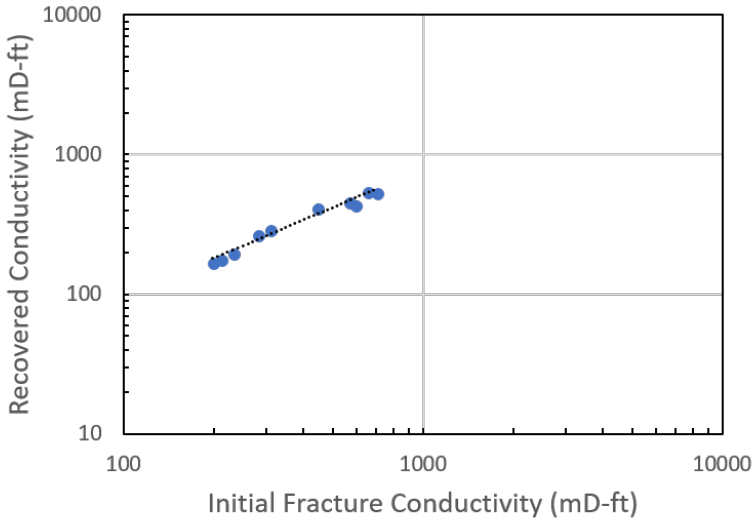

Figure 4.13: Trend for recoverable conductivity versus undamaged conductivity for the Eagle Ford Formation. Adapted from Guerra (2018)

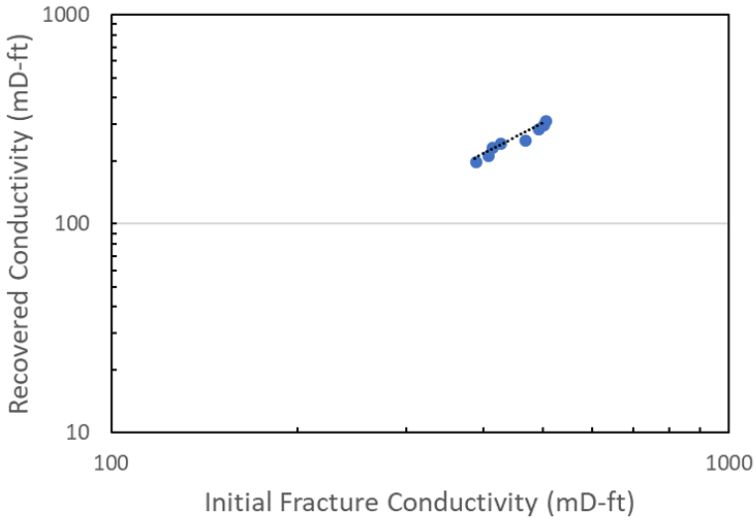

Figure 4.14: Trend for recoverable conductivity versus undamaged conductivity for the Marcellus Formation. Adapted from Guerra (2018)

Where the equation relating recovered fracture conductivity to initial undamaged conductivity in the Eagle Ford is shown in Equation 4.2, and the Marcellus in Equation 4.3.

$$C_{f,recovered} = 1.4496(k_f w_f)^{0.9115} \tag{4.2}$$

$$C_{f,recovered} = 0.024(k_f w_f)^{1.5206} \tag{4.3}$$

Using the proposed approach by Zhang, a correlation has been found to predict recoverable conductivity for the Meramec formation. Using the results for all six water conductivity tests, recovered conductivity after water exposure was plotted against initial undamaged fracture conductivity at 4000 psi on a log-log scale. The produced plot is shown below in Figure 4.15

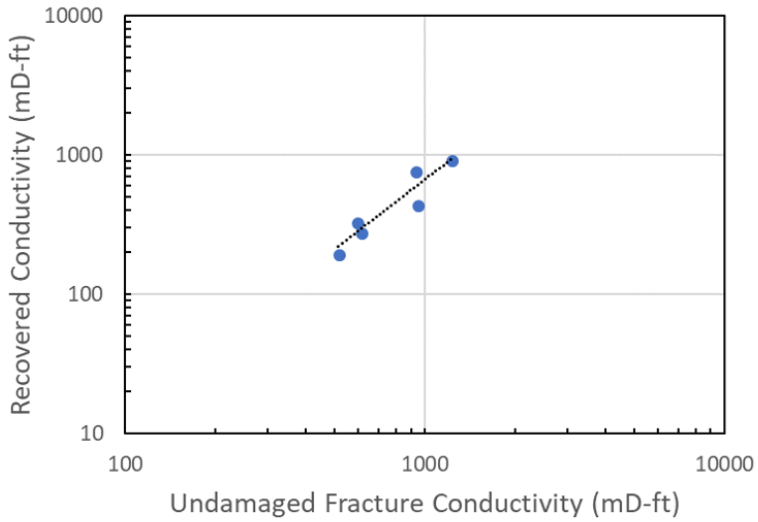

Figure 4.15: Trend for recoverable conductivity versus undamaged conductivity for the Meramec formation.

The resulting equation for these data points is shown below.

$$C_{f,recovered} = 0.007(k_f w_f)^{1.6596} \tag{4.4}$$

In order to compare the results of the Meramec correlation with previous results for the Barnett, Marcellus, and Eagle Ford, undamaged conductivity results for the Meramec were used to plot the resulting recovered conductivity using each correlation. Analyzing the Barnett equation, the resulting conductivity plot predicts recovered conductivities very similar to the actual results. The intersection point between the two equations is at 905 mD-ft, where results for undamaged conductivities larger than this value produced predicted values about 100-200 mD-ft larger than actual results, while undamaged conductivity values lower than 903 mD-ft predicted recovered conductivity values closer to actual values around 20 mD-ft lower to 40 mD-ft larger.

Analyzing the results from the Eagle Ford power law, it has been found that predicting recovered conductivity using this correlation produces overly optimistic recovered fracture conductivity values. The increase from the observed Meramec recovery values ranged from 13 mD-ft to 298 mD-ft. Additionally, predicting recovered conductivity using the Marcellus power law produces overly optimistic recovery values. In the case of the Marcellus, predicted recovered fracture conductivity ranged from 3 mD-ft to 352 mD-ft over the experimentally obtained Meramec results.

These results show that recovered predicted fracture conductivity for the Meramec shale are much lower than the counterpart values for the Barnett, Eagle Ford, and Marcellus Formations.

5. CONCLUSIONS

This thesis presents a study of water damage in fracture conductivity and its impact on downhole core of the Meramec formation. Pre-conductivity test topics such as sample preparation, surface profiling, and sample mineralogy were discussed, along with a detailed procedure of the water damaged fracture conductivity test. The unrecoverable loss in fracture conductivity was investigated as the primary objective. Post-test analyses to characterize this loss in conductivity included a proppant sieve analysis, brittleness characterization, and a correlation was proposed to predict recoverable fracture conductivity due to water damage. The conclusions to this study are presented below:

1. Initial fracture conductivity at 1000 psi shows dependence on the degree of fracture surface roughness and the extent of ΔZ along the fracture surface.

2. Self-channeling of proppant was prevalent for high proppant concentrations at low closure stress, and low concentrations of smaller proppant mesh sizes at low closure stress, which was remedied by starting water conductivity experiments at a closure stress of 2000 psi instead of 1000 psi.

3. The effect of repeated use of core samples was investigated, where it was found dry conductivity increased after repeated use of a sample. For this particular rock, it was observed that a significant portion of the fracture surface was covered in microscopic sand crystals, leading to the theory that recurring tests are tested at an effectively larger proppant concentration.

4. Clay content of the Meramec formation was similar to that of the Marcellus, higher than the Eagle Ford, but lower than the Barnett. This same trend was also found for percent unrecoverable loss in conductivity due to water damage, providing a baseline

for this relatively untested formation to be compared with.

5. Significant proppant crushing was observed, being very prevalent in the low proppant concentrations, helping to contribute to loss in conductivity. Recovered fracture conductivity should provide adequate flow for reservoir fluids when compared to the nanodarcy permeability of the reservoir rock.

6. Based off of previous studies, a correlation was found based upon measured data to calculate recoverable conductivity as a function of initial undamaged conductivity at 4000 psi. This power law was found to behave similarly to the correlation for the Barnett Shale, however actual conductivities were significantly smaller compared to predicted values given by the model for the Eagle Ford and Marcellus Formations.

5.1 Recommendations

Due to the limited number of experiments in this study, further experimentation is needed to solidify the driving mechanisms behind fracture conductivity loss due to water damage in the Meramec formation. Some suggestions for future research include:

1. Perform water fracture conductivity experiments using samples only once to eliminate hysteresis effects.

2. Correlate loss in fracture conductivity with x-ray fluorescence (XRF) to obtain fracture surface mineralogy. XRD is a point-wise measure of bulk mineralogy, and samples sourced from the same core may not be representative of the minerals found on the fracture surface.

3. Collect and analyze effluent water from the fracture for clay ions, which are indicators the clays present in the shale are reacting with the reconstituted brine solution.

4. Perform triaxial core plug tests to obtain Poisson's ratio and Young's modulus for the formation, and attempt a correlation with decline in undamaged fracture conductivity.

5. Test samples using 100 mesh sand to populate the data base with a broader range of proppants for the Meramec formation.

REFERENCES

Akrad, Ola, Miskimins, Jennifer, and Prasad, Manika (Oct. 2011). "The Effects of Fracturing Fluids on Shale Rock Mechanical Properties and Proppant Embedment". In: *Society of Petroleum Engineers*. This paper was presented at the SPE Annual Technical Conference and Exhibition held in Denver, Colorado, USA.

API RP-61: Recommended Practices for Evaluating Short Term Proppant Pack Conductivity (1989). API.

Civan, Faruk (2015). *Petroleum Production Systems*. 3rd. Gulf Professional Publishing.

Cooke Jr, C.E. (Sept. 1973). "Conductivity of Fracture Proppants in Multiple Layers". In: *Society of Petroleum Engineers*. This paper was presented at the SPE-AIME 47^{th} Annual Fall Meeting held in San Antonio, Texas, USA.

Economides, Michael J., Hill, A. Daniel, Zhu, Ding, and Ehlig-Economides, Christine (2012). *Petroleum Production Systems*. 2nd. Cambridge University Press.

Enriquez-Tenorio, Omar (Aug. 2016). "A Comprehensive Study of the Eagle Ford Shale Fracture Conductivity". MA thesis. Texas A&M University.

Fjær, E. and Nes, O.M. (June 2013). "Strength Anisotropy of Mancos Shale". In: *American Rock Mechanics Association*. This paper was presented at the 47^{th} US Rock Mechanics / Geomechanics Symposium held in San Francisco, California, USA.

Fredd, C.N., McConnell, S.B., Boney, C.L., and England, K.W. (Sept. 2001). "Experimental Study of Fracture Conductivity for Water-Fracturing and Conventional Fracturing Applications". In: *Society of Petroleum Engineers*.

Guerra, J., Uribe-Chacon, J., Zhu, D., and Luna-Castillo, E. (May 2017a). "Self-Channeling in Proppant Pack in the Eagle Ford Shale Formation". In: *Society of Petroleum Engineers*.

This paper was presented at the 2017 SPE Latin America and Caribbean Petroleum Conference held in Buenos Aires, Argentina.

Guerra, J., Zhu, D., and Hill, A. Daniel (Jan. 2017b). "Impairment of Fracture Conductivity in the Eagle Ford Shale Formation". In: *Society of Petroleum Engineers*. This paper was presented at the 2017 SPE Hydraulic Fracturing Technology Conference and Exhibition held in The Woodlands, Texas, USA.

Guerra, Jesse (Aug. 2018). "Fracture Conductivity Behavior in Shale Formations". PhD thesis. Texas A&M University.

Guerra, Jesse, Hill, A. Daniel, and Zhu, Ding (July 2017c). "A Comparative Study of the Effects of Clay Content on the Fracture Conductivity of the Eagle Ford Shale and Marcellus Shale Formations". In: *Unconventional Resources Technology Conference*. This paper was presented at the Unconventional Resources Technology Conference held in Austin, Texas, USA.

Jarvie, D.M., Hill, R.J., Ruble, T.E., and Pollastro, R.M. (Apr. 2007). "Unconventional shale-gas systems: The Mississippian Barnett Shale of north-central Texas as one model for thermogenic shale-gas assessment". In: *The American Association of Petroleum Geologists*.

Kassis, Sarah and Sondergeld, Carl (June 2010). "Fracture Permeability of Gas Shale: Effects of Roughness, Fracture Offset, Proppant, and Effective Stress". In: *Society of Petroleum Engineers*. This paper was presented at the CPS/SPE International Oil & Gas Conference and Exhibition held in Beijing, China.

Kias, E., Maharidge, R., and Hurt, R. (Sept. 2015). "Mechanical Versus Mineralogical Brittleness Indices Across Various Shale Plays". In: *Society of Petroleum Engineers*. This paper was presented at the SPE Annual Technology Conference and Exhibition held in Houston, Texas, USA.

Knorr, Ashley F. (May 2016). “The Effect of Rock Properties on Fracture Conductivity in the Eagle Ford”. MA thesis. Texas A&M University.

Li, W., Jin, C., Salviato, M., and Cusatis, G. (July 2015). “Modeling of Failure Behavior of Anisotropic Shale Using Lattice Discrete Particle Model”. In: *American Rock Mechanics Association*. This paper was presented at the 49^{th} US Rock Mechanics / Geomechanics Symposium held in San Francisco, California, USA.

Marpaung, F., Chen, F., Pongthunya, P., Zhu, D., and Hill, A.D. (Sept. 2008). “Measurement of Gel Cleanup in a Propped Fracture with Dynamic Fracture Conductivity Experiments”. In: *Society of Petroleum Engineers*. This paper was presented at the 2008 SPE Annual Technology Conference and Exhibition held in Denver, Colorado, USA.

McDuffie, R.H. (1958). “Lithologic Basis for Correlation of Mississippian Rocks in the Subsurface Between Kansas and North Central Oklahoma”. In: *Oklahoma Academy of Science* 39, pp. 133–135.

McKenna, R.D. (1979). “Petroleum Geology of the Mississippi Lime in Parts of Payne and Pawnee Counties, Oklahoma”. MA thesis. Oklahoma State University.

Montgomery, C. and Smith, M. (2010). “Hydraulic Fracturing: History of an Enduring Technology”. In: *Journal of Petroleum Technology* 62, pp. 26–32.

Montgomery, C. and Smith, M. (2015). *Hydraulic Fracturing*. CRC Press.

Palisch, T., Duenckel, R., Bazan, L., Heidt, H.J., and Turk, B. (Jan. 2007). “Determining Realistic Fracture Conductivity and Understanding its Impact on Well Performance - Theory and Field Examples”. In: *Society of Petroleum Engineers*. This paper was presented at the 2007 SPE Hydraulic Fracturing Technology Conference held in College Station, Texas, USA.

Palisch, T., Vincent, M., and Handren, P. (Aug. 2010). “Slickwater Fracturing: Food for Thought”. In: *SPE Production & Operations*.

Ramurthy, M., Barree, R.D., Kundert, D.P., Petre, E., and Mullen, M. (Nov. 2011). "Surface-Area vs. Conductivity-Type Fracture Treatments in Shale Reservoirs". In: *SPE Production & Operations*.

Rickman, R., Mullen, M., Petre, E., Grieser, B., and Kundert, D. (Sept. 2008). "A Practical Use of Shale Petrophysics for Stimulation Design Optimization: All Shale Plays Are Not Clones of the Barnett Shale". In: *Society of Petroleum Engineers*. This paper was presented at the 2008 SPE Annual Technical Conference and Exhibition held in Denver, Colorado, USA.

Rottmann, K. (May 2011). *Stratigraphic Architecture of the Kinderhookian to Meramecian Series*. Technical presentation given at the Oklahoma Geological Survey Mississippian Play Workshop in Norman, Oklahoma, USA.

Rottmann, K. and Hadaway, S. (Oct. 2012). *The Mississippian of the Mid-Continent; An Overview*. Technical presentation given at the Oklahoma Geological Survey Mississippian & Arbuckle Workshop in Norman, Oklahoma, USA.

Sone, Hiroki and Zoback, Mark D. (Sept. 2013). "Mechanical Properties of Shale-Gas Reservoir Rocks - Part 1: Static and Dynamic Elastic Properties and Anisotropy". In: *Geophysics*.

Thompson, M.E. and Brown, S.R. (Dec. 1991). "The Effect of Anisotropic Surface Roughness on Flow and Transport in Fractures". In: *Journal of Geophysical Research* 96.

Wang, Fred P. and Gale, Julia F.W. (2009). "Screening Criteria for Shale-Gas Systems". In: *The Gulf Coast Association of Geological Societies* 59.

Zhang, J., Zhu, D., and Hill, A.D. (July 2015). "A new theoretical method to calculate shale fracture conductivity based on the population balance equation". In: *Journal of Petroleum Science and Engineering*.

Zhang, Junjing (Aug. 2014). "Creation and Impairment of Hydraulic Fracture Conductivity in Shale Formations". PhD thesis. Texas A&M University.

A. APPENDIX A

A.1 Brittleness Results

Table A.1 shows the brittleness results showing the Jarvie Brittleness Index. The Jarvie BI accounts for quartz, carbonate, and clay content for its calculation with quartz as the primary influence to increasing brittleness.

Sample No.	$BI_{Mi,Jarvie}$
1	0.768
2	0.609
3	0.650
4	0.678
5	0.787
6	0.539

Table A.1: Brittleness results for the Jarvie BI.

Table A.2 shows the brittleness results showing the Kias Brittleness Index. The Kias BI accounts for quartz, carbonate, and clay content for its calculation with quartz as the primary influence to increasing brittleness.

Sample No.	$BI_{Mi,Kias}$
1	0.840
2	0.674
3	0.724
4	0.797
5	0.815
6	0.725

Table A.2: Brittleness results for the Kias BI.